Bifurcation analysis of a vibro-impacting capsule robot in contact with a circular fold

Shan Yin[a], Yao Yan[b], Joseph Páez Chávez[c,d], Yang Liu[a,*]

[a] College of Engineering, Mathematics, and Physical Sciences, University of Exeter, Exeter, UK, EX4 4QF
[b] School of Aeronautics and Astronautics, University of Electronic Sci. and Technology of China, Chengdu, 611731, China
[c] Center for Applied Dynamical Systems and Computational Methods (CADSCOM), Faculty of Natural Sciences and Mathematics, Escuela Superior Politécnica del Litoral, P.O. Box 09-01-5863, Guayaquil, Ecuador
[d] Center for Dynamics, Department of Mathematics, TU Dresden, D-01062 Dresden, Germany

Abstract

The lining of the small intestine consists of a series of circular folds, which is the main source of intestinal resistance for capsule endoscopy. This paper presents an in-depth bifurcation analysis for a vibro-impacting self-propelled capsule robot encountering a circular fold. Using the GPU parallel computing and the path-following techniques, one- and two-parameter bifurcation analyses are performed to reveal the capsule-fold dynamics of a proposed model. It is found that the excitation parameters of the capsule and the fold's mechanical properties can significantly influence the bifurcation scenarios. Then basin stability analysis is further conducted to uncover the capsule-fold dynamics from a probability perspective. Numerical results indicate that the period-one motion of the capsule-fold interaction and the crossing motion can dominate the global dynamics of the system in the small and large excitation amplitude regions, respectively. Once the mechanical properties of the circular fold are varied, a significant change in multistability is also observed and demonstrated via the basins of attraction. The results presented in this work are intended to provide a solid basis for the locomotion control of the capsule robot in the small intestine when encountering different types of circular folds.

Keywords: Vibro-impact; Non-smooth system; Self-propelled capsule; Bifurcation analysis; Multistability.

1. Introduction

Mechanical systems involving non-smooth phenomena, such as impact and friction can be widely found in many engineering applications. For example, the friction and impact contacts arising in robots can be used for self-propulsion in complex environments, providing the ability for accurate positioning and directional locomotion [1, 2]. The impact contact occurring in indenter-rock interactions of the percussive drilling systems can significantly magnify the input force and promote drilling efficiency [3]. The impact contact appearing in the hinge structures can induce strong forces and vibrations, influencing the motion stability and the pointing accuracy of large-scaled spacecraft [4]. The wheel-rail interactions associated with impact and friction might induce strong nonlinear resonances, leading to rail corrugation and affecting the safety of high-speed trains [5]. To improve the performances of mechanical systems involving impact or friction, a further insight into the instability mechanisms of these systems is required. Indeed, the key point of developing such instability mechanisms should be focused on the nonlinear phenomena observed in the non-smooth systems [6, 7], e.g., bifurcations, chaos, and multistability. For example, Wang et al. [8] proposed an analytical approach to predict the self-excited stick-slip whirling oscillations in a general rotor/stator rubbing system by taking the dry friction contact into consideration. Yadav et al. [9] investigated the nonlinear dynamics of a spring–dashpot system by considering the friction and backlash simultaneously. Moreover, the analytical study on the phase-space trajectories also indicated

*Corresponding author. Tel: +44(0)1392-724654, e-mail: y.liu2@exeter.ac.uk.

the occurrence of novel grazing-sliding bifurcations. Stefani et al. [10–12] presented detailed numerical and experimental analyses on the response scenarios in a single-degree-of-freedom impact oscillator with two unilateral dissipative and deformable constraints and discussed parametric influences on the system dynamics. Afebu et al. [13] proposed a data-driven method to learn the complexity of co-existing impact oscillations and predicted the steady responses of an impact oscillator from limited transient data by using the long short term memory network. Saunders et al. [14] discussed the effects of the geometric and non-smooth nonlinearities on the bifurcations and the secondary resonances of a Duffing-free play system. Li et al. [15] presented a non-smooth Melnikov analysis and experimental validation for a class of bistable nonlinear impact oscillators with bilateral rigid constraints. Geng et al. [16] proposed a novel nonlinear energy sink with piecewise linear springs to reduce the vibration amplitudes of the primary structure, enhancing the potential application of the system in engineering. Staunton et al. [17] derived the zero-time discontinuity mappings for the stability and bifurcation analysis of periodic motions in the stochastic non-smooth systems, where the stochastically oscillating boundaries or the stochastic imperfections on the discontinuity boundaries were considered. Simpson et al. [18] presented a comparative study between the Poincaré map of an impact oscillator and the corresponding Nordmark map for the problem of large-amplitude chaos and pointed out that the neglected higher-order terms in the Nordmark map could have a significant influence on revealing the global dynamics of the systems. Tan et al. [19] investigated the near-grazing bifurcations of a single-degree-of-freedom impact oscillator with two-sided elastic constraints and designed a proper framework using deep reinforcement learning to stabilize the non-stationary bifurcation responses close to grazing.

Among the above non-smooth nonlinear mechanical systems, the self-propelled locomotion robots have attracted a great attention from the research community in recent years, see e.g., [1, 2, 20–29], since such systems can move efficiently in complex environments. In the past decade, various locomotion mechanisms have been developed to provide active propulsive force for driving robots. For example, Xu and Fang [1] summarized the recent progress on the vibration-driven locomotion systems from the aspects of utilising the stick-slip effect, exploiting the bistable actuation and incorporating multiple internal oscillators. Xue et al. [22] proposed the design criteria of the driving amplitude and frequency for a vibration-driven locomotion system by using the Pareto front method to obtain a high locomotion velocity while consuming low energy. Madani et al. [24] studied the optimal actuation configuration for the rotating spiral capsule driven by an external rotational magnetic field through the genetic algorithm. Kim et al. [25] developed a prototype of the earthworm-like capsule robot, which was driven by the impact-based piezo actuator. Park et al. [26] designed the paddle-based capsule which was driven by multiple synchronised legs and a linear actuator. Quirini et al. [27] proposed a legged capsule robot actuated by a brushless minimotor and revealed the actuation and transmission mechanisms. Guo et al. [2] presented the experimental study on a vibro-impacting capsule in mesoscale and discussed the feasibility of such a capsule prototype under different frictional environments. Nguyen et al. [28] demonstrated the effects of various dry and isotropic friction levels on the progression and dynamic response of a vibro-impacting capsule system by bifurcation analysis and experimental validation. Miao et al. [29] studied the speed optimization and reliability analysis of a capsule robot by using the combination of Six Sigma, Multi-Island Genetic and Monte Carlo algorithms.

In this paper, a circular fold will be considered as the obstacle of locomotion of a vibro-impacting self-propelled capsule robot moving in the small intestine for endoscopic diagnosis. The vibro-impacting self-propelled capsule robot [30–32] is a non-smooth dynamical system driven by its internal vibration and impact in a rectilinear manner in the presence of environmental resistance. Previous studies [2, 23, 30–33] only considered the capsule's dynamics on a flat surface without the consideration of intestinal anatomy. While considering the lining of the small intestine that consists of a series of circular folds in different sizes, dynamics and locomotion of the capsule will be significantly influenced by these folds. Thus, the present work will study the capsule's dynamics when encountering various types of circular folds and provide locomotion control for the capsule robot moving in the small intestine. In particular, this paper provides detailed one- and two-parameter bifurcation analyses of the capsule-fold dynamics under four different fold cases. To perform such a bifurcation analysis, the contact force of capsule-fold interaction [34, 35] will be firstly approximated as a piecewise smooth nonlinear restoring force via interpolation. Then bifurcation analysis will be conducted by using the GPU parallel computing and path-following techniques [36–38].

Indeed, the GPU parallel computing method can provide an initial view of the capsule-fold dynamics, while the path-following analysis is used to zoom-in into drastic changes in the dynamical behavior upon subtle perturbations of the system parameters. The combination of these numerical approaches will be employed to investigate the effect of the excitation parameters of the capsule (e.g., duty cycle and amplitude) and the fold's mechanical properties (e.g., height and elastic modulus) on the capsule-fold dynamics and the bifurcation scenarios. Thereafter, basin stability analysis will be performed to measure the stability of a particular a from a probability perspective. Special attention will be given to the period-one motion with capsule-fold contact and study how it is affected by the fold's properties when the excitation amplitude of the capsule robot is small. Moreover, one-parameter basin stability analysis will be carried out so as to determine the presence of multistability in the system along with the change of excitation amplitude, considering four fold cases with different mechanical properties under certain system parameters.

The contribution of the present work is twofold. On the one hand, this paper presents detailed one- and two-parameter bifurcation analyses of the capsule-fold dynamics under different fold mechanical properties, uncovering the instability mechanisms of the period-one impact motion from a local point of view. Such results can provide essential guidance for the locomotion control of the capsule robot in the small intestine. On the other hand, this paper presents basin stability analysis to further characterise the capsule-fold dynamics from a global perspective, indicating the main attractors in different parameter regions. More importantly, the basin stability analysis also reveals a significant change in multistability when the capsule encounters different circular folds. Indeed, such a correlation between the dynamical characteristics and the fold's mechanical properties can provide the potential of utilising the multistability for the detection of various types of circular folds.

The rest of this paper is organized as follows. In Section 2, the mathematical modelling of the vibro-impacting capsule encountering a circular fold on the small intestinal substrate is presented. To obtain the desired mathematical model, the capsule-intestine interaction is studied firstly in Section 2.1. Then the generic model of the vibro-impacting capsule robot is introduced in Section 2.2, and the contact force between the capsule and the circular fold is approximated as a piecewise smooth nonlinear restoring force through interpolation. To perform the bifurcation analysis, a dimensionless transformation of the capsule-fold model is further conducted in Section 2.3. On this basis, the desired bifurcation analysis can be performed and interpreted in Section 3. In Section 3.1, a two-parameter bifurcation analysis is firstly conducted to provide some initial insights into the capsule-fold dynamics. Then a detailed one-parameter bifurcation analysis is presented in Section 3.2 to further understand the two-parameter numerical results. Thereafter, basin stability analysis is conducted in Section 3.3 to better reveal the multistability of the capsule-fold dynamics. The paper finalizes with Section 4, where the main conclusions of this work are drawn.

2. Modelling of the capsule-fold dynamics

2.1. Modelling of the capsule-intestine interaction

A capsule moving in the small intestine is subjected to complex environmental interaction. To simplify its mathematical model displayed in Fig. 1(a) for analytical study, it is assumed that the capsule can only translate in the xoy plane. Thus the capsule in Fig. 1(b) does not tilt when it crosses the fold, see Fig. 1(d). This assumption was proposed and experimentally validated by Sliker et al. [34]. Given the tissue softness, the capsule is regarded as rigid and tissue's incompressible isotropic deformation conforms to the capsule profile [34, 35], see Fig. 1(c).

As displayed in the front view of the cross section A-A in Fig. 1(b), the capsule moving rightward has hemispheric tail and head with a radius of R mm and a cylindrical body with a length of L mm. Due to the capsule's gravity, it penetrates into the tissue with a depth of $\delta_{\max}$ mm. The small intestine has a thickness of H mm, with a circular fold located at x_b mm. The fold has a height of h mm and a width of w mm, and can be mathematically described as follows

$$f(x) = \begin{cases} h\cos\left(\frac{x-x_{\mathrm{b}}}{2w}\pi\right), & |x-x_{\mathrm{b}}| \le w, \\ 0, & |x-x_i| > w. \end{cases} \tag{1}$$

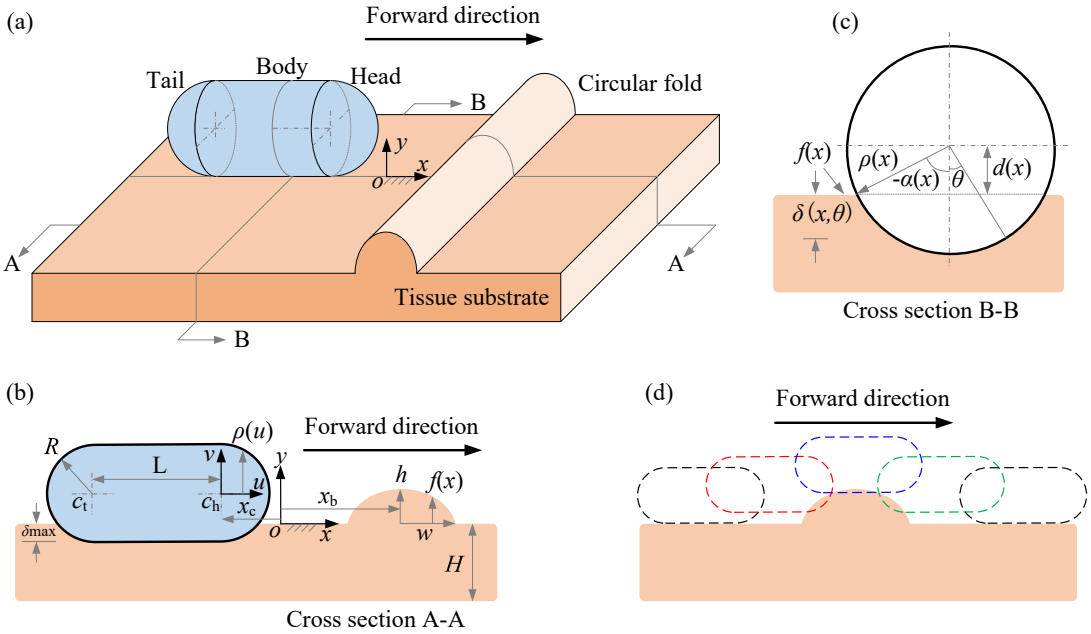

Figure 1: (a) 3D schematic diagram of the capsule moving on an intestinal substrate with a circular fold. (b) Front view and (b) side view of the interaction between the capsule and the small intestine. (d) The assumption that the capsule can only translate without any rotation during its crossing [34].

Letting the centre of capsule head located at x_c, cross section B-B in Fig. 1(c) for $x \in [x_c - L - R, x_c + R]$ shows a round side view of the capsule with a radius of

$$\rho(x_c, x) = \begin{cases} \sqrt{R^2 - (x - x_c)^2}, & x_c < x \le x_c + R, \\ R, & x_c - L \le x \le x_c, \\ \sqrt{R^2 - (x - x_c + L)^2}, & x_c - R - L \le x < x_c - L. \end{cases} \tag{2}$$

At the same position, the vertical distance from the capsule's central axis to the tissue surface is given by

$$d(\delta_{\max}, x) = R - \delta_{\max} - f(x). \tag{3}$$

There will be no capsule-intestine interaction if the distance is larger than the radius of the capsule's section, i.e., $d(\delta_{\max}, x) > \rho(x_c, x)$. For $d(\delta_{\max}, x) \le \rho(x_c, x)$, the capsule and the tissue have a limited contact angle, $\theta \in [-\alpha(x_c, \delta_{\max}, x), \alpha(x_c, \delta_{\max}, x)]$, where the limit is

$$\alpha(x_c, \delta_{\max}, x) = \arccos\left(\min\left(1, \frac{d(\delta_{\max}, x)}{\rho(x_c, x)}\right)\right). \tag{4}$$

Given the contact angle, the capsule's bottom can be mathematically described as

$$p(x_c, \delta_{\max}, x, \theta) = R - \delta_{\max} - \rho(x_c, x)\cos(\theta). \tag{5}$$

In the area of capsule-tissue interaction, the small intestine deforms from its own shape function to the capsule's, yielding the deformation

$$\delta(x_c, \delta_{\max}, x, \theta) = \max\left(0, f(x) - p(x_c, \delta_{\max}, x, \theta)\right). \tag{6}$$

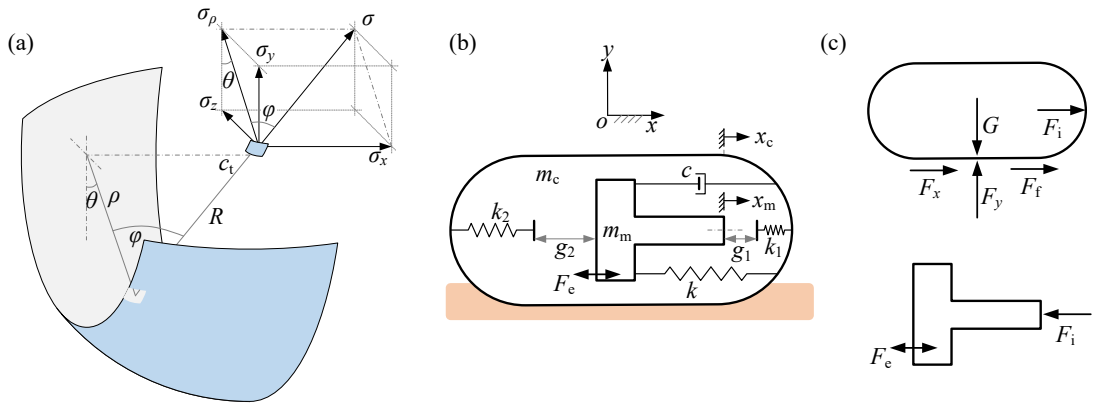

Figure 2: (a) Pressure of the small intestine exerted on the capsule. (b) The capsule has an inner mass interacting with the shell via a primary spring and two impact constraints. (c) Free-body diagrams of the capsule shell and the inner mass.

This deformation is then divided by the original thickness of the substrate for the strain as follows

$$\epsilon(x_c, \delta_{\max}, x, \theta) = \frac{\delta(x_c, \delta_{\max}, x, \theta)}{H + f(x)}. \tag{7}$$

The corresponding stress is

$$\sigma(x_c, \delta_{\max}, x, \theta) = \epsilon(x_c, \delta_{\max}, x, \theta)E, \tag{8}$$

where E is Young's module of the tissue. As seen in Fig. 2(a), stress exerts normal pressure on the capsule shell and its $x-$ and $y-$components can be obtained by using

$$\begin{aligned} \sigma_x(x_c, \delta_{\max}, x, \theta) &= \sigma(x_c, \delta_{\max}, x, \theta)\sin(\varphi), \\ \sigma_y(x_c, \delta_{\max}, x, \theta) &= \sigma(x_c, \delta_{\max}, x, \theta)\cos(\varphi)\cos(\theta), \end{aligned} \tag{9}$$

where

$$\varphi(x) = \begin{cases} -\sin^{-1}\left(\frac{x-x_c}{R}\right), & x_c < x \le x_c + R, \\ 0, & x_c - L \le x \le x_c, \\ -\sin^{-1}\left(\frac{x-x_c+L}{R}\right), & x_c - R - L \le x < x_c - L, \end{cases} \tag{10}$$

is the angle of anticlockwise rotation from R to ρ shown in Fig. 2(a).

In the vertical direction, as displayed in Fig. 2(c), the capsule's gravity is cancelled by the reaction force exerted by the tissue on the capsule shell in y-direction,

$$F_y(x_c, \delta_{\max}) = G, \tag{11}$$

and $F_y(x_c, \delta_{\max})$ can be obtained by integrating $\sigma_y(x_c, \delta_{\max}, x, \theta)$ over the capsule shell as follows

$$F_y(x_c, \delta_{\max}) = \int_{x_c - L - R}^{x_c + R} \int_{-\alpha(x_c, \delta_{\max}, x)}^{\alpha(x_c, \delta_{\max}, x)} \sigma_y(x_c, \delta_{\max}, x, \theta)\rho(x)\mathrm{d}\theta \frac{\mathrm{d}x}{\cos(\varphi(x))}. \tag{12}$$

For a given capsule position, x_c, the depth of capsule penetration into the tissue, $\delta_{\max}$, can be obtained by numerically solving Eqs. (11) and (12). Therefore, $\delta_{\max}(x_c)$ can be regarded as an implicit function of x_c. With this depth, the horizontal reaction force is obtained by integrating $\sigma_x(x, \theta)$ as follows

$$F_x(x_c) = \int_{x_c - L - R}^{x_c + R} \int_{-\alpha(x_c, \delta_{\max}(x_c), x)}^{\alpha(x_c, \delta_{\max}(x_c), x)} \sigma_x(x_c, \delta_{\max}(x_c), x, \theta)\mathrm{d}\theta \frac{\mathrm{d}x}{\cos(\varphi(x))}. \tag{13}$$

2.2. Modelling of the vibro-impacting capsule robot

To drive the capsule shell to move rightward, an inner mass inside the shell is periodically driven by an external excitation as follows

$$F_{\mathrm{e}} = \begin{cases} P_{\mathrm{d}}, & \mod(t,T) \in [0, DT], \\ 0, & \text{otherwise}, \end{cases} \tag{14}$$

where $\mod(t,T)$ indicates t modulo T, and P_{d}, T and $D \in (0,1)$ are the amplitude, period, and duty cycle ratio of the square wave excitation, respectively. As depicted in Fig. 2(b), the inner mass interacts with the capsule shell via a primary damped spring which has a stiffness k N/m and a damping of c Ns/m, and two impact constraints in front and behind the inner mass which are of stiffness, k_1 N/m and k_2 N/m, and gaps, g_1 mm and g_2 mm, respectively. Thus the interactive force between the inner mass and the capsule shell can be represented by the following piecewise linear function

$$F_{\mathrm{i}} = \begin{cases} kx_{\mathrm{r}} + cv_{\mathrm{r}} + k_1\left(x_{\mathrm{r}} - g_1\right), & \text{if } x_{\mathrm{r}} > g_1, \\ kx_{\mathrm{r}} + cv_{\mathrm{r}}, & \text{if } -g_2 \le x_{\mathrm{r}} \le g_1, \\ kx_{\mathrm{r}} + cv_{\mathrm{r}} + k_2\left(x_{\mathrm{r}} + g_2\right), & \text{if } x_{\mathrm{r}} < -g_2, \end{cases} \tag{15}$$

where $x_{\mathrm{r}} = x_{\mathrm{m}} - x_{\mathrm{c}}$ and $v_{\mathrm{r}} = \dot{x}_{\mathrm{m}} - \dot{x}_{\mathrm{c}}$ are the displacement and velocity of the inner mass relative to the shell.

Besides the interactive force, F_{i}, the capsule shell is subjected to the reaction from the small intestine, including F_x and Coulomb friction F_{f}, where the frictional force can be represented as

$$F_{\mathrm{f}} = \begin{cases} -\operatorname{sign}(\dot{x}_{\mathrm{c}})\mu G, & \text{if } \dot{x}_{\mathrm{c}} \neq 0, \\ -\operatorname{sign}(F_{\mathrm{i}} + F_x)\mu G, & \text{if } \dot{x}_{\mathrm{c}} = 0 \text{ and } \operatorname{abs}\left(F_{\mathrm{i}} + F_x\right) \ge \mu G, \\ -F_{\mathrm{i}} - F_x, & \text{if } \dot{x}_{\mathrm{c}} = 0 \text{ and } \operatorname{abs}\left(F_{\mathrm{i}} + F_x\right) < \mu G, \end{cases} \tag{16}$$

where $\operatorname{sign}(*)$ and $\operatorname{abs}(*)$ are the sign and absolute functions of $*$, and μ is the frictional coefficient. To sum up, the dynamics of the capsule shell and the inner mass shown in Fig. 2(c) are governed by

$$\begin{cases} m_{\mathrm{m}}\ddot{x}_{\mathrm{m}} = F_{\mathrm{e}} - F_{\mathrm{i}}, \\ m_{\mathrm{c}}\ddot{x}_{\mathrm{c}} = F_{\mathrm{i}} + F_x + F_{\mathrm{f}}. \end{cases} \tag{17}$$

It should be noted that a direct application of the resistant force F_x expressed by Eq. (13) for numerical simulation will be extremely time-consuming due to the numerical integration of Eqs. (12) and (13), and iteratively solving Eq. (11). Alternatively, an interpolation approximation of the resistant force F_x is conducted for the purpose of convenience. It is assumed that the capsule contacts a nonlinear spring with a restoring force in the following form

$$\begin{aligned} F_{\mathrm{b}}(x_{\mathrm{c}}) = &-(H(x_{\mathrm{c}} - g_{\mathrm{b}}) - H(x_{\mathrm{c}} - (g_{\mathrm{b}} + l_{\mathrm{b}})))F_{\mathrm{b1}}(x_{\mathrm{c}}) - (H(x_{\mathrm{c}} - (g_{\mathrm{b}} + l_{\mathrm{b}})) - H(x_{\mathrm{c}} - (g_{\mathrm{b}} + m_{\mathrm{b}})))F_{\mathrm{b2}}(x_{\mathrm{c}}) \\ &+ (H(x_{\mathrm{c}} - g_\ell) - H(x_{\mathrm{c}} - (g_\ell + m_{\mathrm{b}} - l_{\mathrm{b}})))F_{\mathrm{b3}}(x_{\mathrm{c}}) \\ &+ (H(x_{\mathrm{c}} - (g_\ell + m_{\mathrm{b}} - l_{\mathrm{b}})) - H(x_{\mathrm{c}} - (g_\ell + m_{\mathrm{b}})))F_{\mathrm{b4}}(x_{\mathrm{c}}), \end{aligned} \tag{18}$$

where $H(\cdot)$ stands for the Heaviside step function and nonlinear functions F_{bj} are defined as follows

$$\begin{aligned} F_{\mathrm{b1}}(x_{\mathrm{c}}) &= \beta_0(x_{\mathrm{c}} - g_{\mathrm{b}}) + \beta_1(x_{\mathrm{c}} - g_{\mathrm{b}})^2 + \beta_2(x_{\mathrm{c}} - g_{\mathrm{b}})^3, \\ F_{\mathrm{b2}}(x_{\mathrm{c}}) &= \eta_0(x_{\mathrm{c}} - (g_{\mathrm{b}} + m_{\mathrm{b}})) + \eta_1(x_{\mathrm{c}} - (g_{\mathrm{b}} + m_{\mathrm{b}}))^2 + \eta_2(x_{\mathrm{c}} - (g_{\mathrm{b}} + m_{\mathrm{b}}))^3, \\ F_{\mathrm{b3}}(x_{\mathrm{c}}) &= -\eta_0(x_{\mathrm{c}} - g_\ell) + \eta_1(x_{\mathrm{c}} - g_\ell)^2 - \eta_2(x_{\mathrm{c}} - g_\ell)^3, \\ F_{\mathrm{b4}}(x_{\mathrm{c}}) &= -\beta_0(x_{\mathrm{c}} - (g_\ell + m_{\mathrm{b}})) + \beta_1(x_{\mathrm{c}} - (g_\ell + m_{\mathrm{b}}))^2 - \beta_2(x_{\mathrm{c}} - (g_\ell + m_{\mathrm{b}}))^3. \end{aligned} \tag{19}$$

In Eqs. (18) and (19), g_b and g_l represent the capsule positions where its head and tail start to interact with the fold, respectively. After the head is engaged with the fold, the maximum horizontal resistance force is achieved when the capsule further moves forward with a distance of l_b, and the interaction ends with a distance of m_b. Detailed illustration of these parameters are displayed in Fig. 3.

In the present work, the parameters of the capsule robot and the small intestine are shown in Table 1, and the four different groups of fold parameters are shown in Table 2, where their corresponding fitting parameters for Eqs. (18) and (19) are presented in Table 3. It is worth noting that all these capsule and intestine parameters were obtained from our experiments reported in [23, 33], and the dimensions of the circular folds used in the present work are reasonable according to Barducci et al. [39]. Taking Case 1 of Table 2 as an example, the resistant force $F_x(x_c)$ generated by Eq. (13) and its interpolation approximation $F_b(x_c)$ by Eqs. (18) and (19) are plotted in Fig. 3, showing a good agreement.

Table 1: Parameters of the capsule and the small intestine [23, 33].

Parameter	Symbol	Unit	Value
Capsule radius	R	mm	5.50
Capsule length	L	mm	15
Damping	c	Ns/m	0.0156
Right gap	g_1	mm	1.6
Left gap	g_2	mm	0
Stiffness of the primary spring	k	N/m	62
Stiffness of the second spring	k_1	N/m	27900
Stiffness of the tertiary spring	k_2	N/m	53500
Frictional coefficient	μ	-	0.2293
Thickness of the small intestine	H	mm	0.69
Mass of the magnet	m_m	g	1.8
Mass of the capsule	m_c	g	1.67
Gravity	G	mN	$(m_m + m_c) \times 9.81$
Duty cycle	D	-	$[0.3, 0.6]$
Excitation amplitude	P_d	mN	$[\mu G, 4\mu G]$
Excitation period	T	s	0.05

Table 2: Parameters of various folds [23, 33].

Parameter	Symbol	Unit	Case 1	Case 2	Case 3	Case 4
Location	x_b	mm	12.66	12.66	12.66	12.66
Height	h	mm	1.67	1.67	2.34	2.34
Width	w	mm	1.665	1.665	1.545	1.545
Young's Module	E	kPa	25	10	25	10

Table 3: Fitting parameters of the fold's resistant force under various folds

Symbol	Unit	Case 1	Case 2	Case 3	Case 4
β_0	N/m	-9.111e-2	2.046	1.811	2.495
β_1	N/m^2	3.918e+04	1.116e+04	5.018e+04	1.55e+04
β_2	N/m^3	-1.925e+07	-4.301e+06	-2.42e+07	-5.782e+06
η_0	N/m	6.945e-1	1.004	-0.05391	0.9442
η_1	N/m^2	2.183e+03	1936	1896	2192
η_2	N/m^3	2.106e+05	1.625e+05	1.377e+05	1.871e+05
g_b	m	8.31e-3	8.27e-3	7.83e-3	7.79e-3
l_b	m	1.033e-3	1.904e-3	0.9944e-3	1.756e-3
m_b	m	5.31e-3	5.62e-3	5.67e-3	5.96e-3
g_l	m	26.71e-3	26.44e-3	26.83e-3	26.58e-3

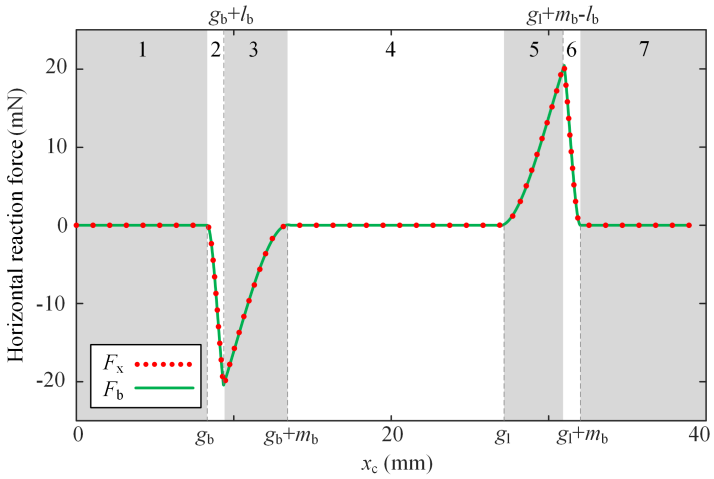

Figure 3: Horizontal resistant force (red dots), $F_x(x_c)$, and its approximation (blue solid), $F_b(x_c)$ for $R = 5.5$ mm, $L = 15$ mm, $m_m + m_c = 3.47$ g, $E = 25$ kPa, $H = 0.69$ mm, $x_b = 12.66$ mm, $h = 1.67$ mm, and $w = 1.665$ mm, which corresponds to the approximation parameters of $g_b = 8.31$ mm, $l_b = 1.033$ mm, $m_b = 5.31$ mm, $g_l = 26.71$ mm, $\beta_0 = -0.09111$ mN/mm, $\beta_1 = 39.18$ mN/mm^2, $\beta_2 = -19.25$ mN/mm^3, $\eta_0 = 0.6945$ mN/mm, $\eta_1 = 2.183$ mN/mm^2, $\beta_2 = 0.2106$ mN/mm^3. In addition, seven phases of capsule-fold interaction were defined as marked by 1-7 to indicate the position of the capsule's periodic motion relative to the fold's location.

2.3. Mathematical formulation for path-following analysis

For the numerical analysis of the capsule system (17), it is convenient to consider the following nondimensional parameters and variables,

$$
\begin{aligned}
&\Omega_0 = \sqrt{\frac{k}{m_m}}, \quad \tau = \Omega_0 t, \quad \widetilde{T} = \Omega_0 T, \quad \xi = \frac{c}{2m_m\Omega_0}, \quad A = \frac{P_d}{\mu G},\\
&\widetilde{x}_m = \frac{k}{\mu G}x_m, \quad \widetilde{x}_c = \frac{k}{\mu G}x_c, \quad \widetilde{x}_r = \frac{k}{\mu G}x_r, \quad \widetilde{g}_1 = \frac{k}{\mu G}g_1, \quad \widetilde{g}_2 = \frac{k}{\mu G}g_2,\\
&\widetilde{g}_b = \frac{k}{\mu G}g_b, \quad \widetilde{l}_b = \frac{k}{\mu G}l_b, \quad \widetilde{g}_\ell = \frac{k}{\mu G}g_\ell, \quad \widetilde{m}_b = \frac{k}{\mu G}m_b, \quad \gamma = \frac{m_m}{m_c},\\
&\widetilde{k}_1 = \frac{k_1}{k}, \quad \widetilde{k}_2 = \frac{k_2}{k}, \quad \widetilde{\beta}_0 = \frac{\beta_0}{k}, \quad \widetilde{\beta}_1 = \frac{\beta_1\mu G}{k^2}, \quad \widetilde{\beta}_2 = \frac{\beta_2(\mu G)^2}{k^3},\\
&\widetilde{\eta}_0 = \frac{\eta_0}{k}, \quad \widetilde{\eta}_1 = \frac{\eta_1\mu G}{k^2}, \quad \widetilde{\eta}_2 = \frac{\eta_2(\mu G)^2}{k^3}.
\end{aligned}
\tag{20}
$$

In what follows, we will denote by $z = (x_m, v_m, x_r, v_r, s)^T \in \mathbb{R}^5$ and $\lambda = (T, A, D, \gamma, k_1, k_2, \xi, g_1, g_2, g_b, l_b, g_\ell, m_b, \beta_0, \beta_1, \beta_2, \eta_0, \eta_1, \eta_2) \in \times\mathbb{R}^{19}$ the state variables and parameters of the system, respectively, where the tildes have been dropped for the sake of simplicity. In this framework, the capsule motion can be described by the following non-dimensional form.

$$
\begin{aligned}
z' &= \begin{pmatrix} v_m \\ Af_e - f_0 - H_{k_1}f_1 - H_{k_2}f_2 \\ v_r \\ Af_e - f_0 - H_{k_1}f_1 - H_{k_2}f_2 - \gamma|H_{vel}|\left(f_0 + H_{k_1}f_1 + H_{k_2}f_2 + F_b(x_c) - H_{vel}\right) \\ 1 \end{pmatrix} \\
&= f_{CAP}(z, \lambda, H_{k_1}, H_{k_2}, H_{vel}, H_{b1}, H_{b2}, f_e),
\end{aligned}
\tag{21}
$$

where the prime symbol denotes derivative with respect to the non-dimensional time τ and $f_0 = x_r + 2\xi v_r$, $f_1 = k_1(x_r - g_1)$, $f_2 = k_2(x_r + g_2)$. In addition, the fold's resistant force function F_b to be used in the

current implementation will incorporate special flags $H_{\mathrm{b}1}$ and $H_{\mathrm{b}2}$ so as to identify operation modes for the range $x_{\mathrm{c}} \leq g_{\mathrm{b}} + m_{\mathrm{b}}$, which correspond to the situation where the capsule hits the circular fold and does not step on it entirely. In this case, the resistant force function of the fold is given by

$$\begin{aligned} F_{\mathrm{b}}(x_{\mathrm{c}}) = &-H_{\mathrm{b}1}F_{\mathrm{b}1}(x_{\mathrm{c}}) - H_{\mathrm{b}2}F_{\mathrm{b}2}(x_{\mathrm{c}}) + (H(x_{\mathrm{c}} - g_\ell) - H(x_{\mathrm{c}} - (g_\ell + m_{\mathrm{b}} - l_{\mathrm{b}})))F_{\mathrm{b}3}(x_{\mathrm{c}}) \\ &+ (H(x_{\mathrm{c}} - (g_\ell + m_{\mathrm{b}} - l_{\mathrm{b}})) - H(x_{\mathrm{c}} - (g_\ell + m_{\mathrm{b}})))F_{\mathrm{b}4}(x_{\mathrm{c}}). \end{aligned}$$

Note that in model (21) we have introduced an additional variable s, whose purpose is to map the time into the state space. This variable will be allowed to vary within the excitation period $[0, T]$, due to which we will implement the reset rule

$$s(\tau^+) = s(\tau^-) - T, \quad \text{whenever} \quad s(\tau) = T, \tag{22}$$

assuming that s has started in $[0, T]$. On the other hand, model (21) includes the flags H_{k_1}, H_{k_2}, H_{vel}, $H_{\mathrm{b}1}$, $H_{\mathrm{b}2}$ and f_{e}, which represent discrete variables defining the operation modes of the system, according to the rules

$$H_{\mathrm{k}_1} = \begin{cases} 1, & x_{\mathrm{r}} - g_1 \geq 0, \quad \text{(contact with } k_1\text{)}, \\ 0, & x_{\mathrm{r}} - g_1 < 0, \quad \text{(no contact)}, \end{cases} \tag{23}$$

$$H_{\mathrm{k}_2} = \begin{cases} 1, & x_{\mathrm{r}} + g_2 \leq 0, \quad \text{(contact with } k_2\text{)}, \\ 0, & x_{\mathrm{r}} + g_2 > 0, \quad \text{(no contact)}, \end{cases} \tag{24}$$

$$H_{\mathrm{b}1} = \begin{cases} 1, & g_{\mathrm{b}} < x_{\mathrm{c}} \leq g_{\mathrm{b}} + l_{\mathrm{b}}, \quad \text{(contact with fold with force } F_{\mathrm{b}1} \text{ on)}, \\ 0, & \text{otherwise}, \quad \text{(force } F_{\mathrm{b}1} \text{ off)}, \end{cases} \tag{25}$$

$$H_{\mathrm{b}2} = \begin{cases} 1, & g_{\mathrm{b}} + l_{\mathrm{b}} < x_{\mathrm{c}} \leq g_{\mathrm{b}} + m_{\mathrm{b}}, \quad \text{(contact with fold with force } F_{\mathrm{b}2} \text{ on)}, \\ 0, & \text{otherwise}, \quad \text{(force } F_{\mathrm{b}2} \text{ off)}, \end{cases} \tag{26}$$

$$f_{\mathrm{e}} = \begin{cases} 1, & 0 \leq s < DT, \quad \text{(forcing on)}, \\ 0, & DT \leq s < T, \quad \text{(forcing off)}, \end{cases} \tag{27}$$

$$H_{\mathrm{vel}} = \begin{cases} 0, & v_{\mathrm{c}} = 0 \ \text{ and } \ \left| f_0 + H_{\mathrm{k}_1} f_1 + H_{\mathrm{k}_2} f_2 + F_{\mathrm{b}}(x_{\mathrm{c}}) \right| \leq 1, \quad \text{(capsule stationary)}, \\ 1, & v_{\mathrm{c}} > 0 \ \text{ or } \ \left(v_{\mathrm{c}} = 0 \ \text{ and } \ f_0 + H_{\mathrm{k}_1} f_1 + H_{\mathrm{k}_2} f_2 + F_{\mathrm{b}}(x_{\mathrm{c}}) > 1 \right), \quad \text{(forward motion)}, \\ -1, & v_{\mathrm{c}} < 0 \ \text{ or } \ \left(v_{\mathrm{c}} = 0 \ \text{ and } \ f_0 + H_{\mathrm{k}_1} f_1 + H_{\mathrm{k}_2} f_2 + F_{\mathrm{b}}(x_{\mathrm{c}}) < -1 \right), \quad \text{(backward motion)}, \end{cases} \tag{28}$$

where $x_{\mathrm{c}} = x_{\mathrm{m}} - x_{\mathrm{r}}$ and $v_{\mathrm{c}} = v_{\mathrm{m}} - v_{\mathrm{r}}$. Note that in the expressions above, the term $f_{\mathrm{mc}} = f_0 + H_{\mathrm{k}_1} f_1 + H_{\mathrm{k}_2} f_2 + F_{\mathrm{b}}(x_{\mathrm{c}})$ represents the force acting on the capsule from the inner mass and the fold. Therefore, if the capsule is stationary, whenever the force f_{mc} becomes greater than 1 or smaller than -1, the capsule will move forward or backward, respectively. For the numerical implementation, the discrete variables defined in (23)–(28) will be used to identify the specific operation mode of the capsule. Every operation mode will be associated with a quartet $\{\Sigma, \Delta, \Theta, \Gamma\}$, where $\Sigma \in \{\mathrm{NCk}, \mathrm{Ck1}, \mathrm{Ck2}\}$ (no contact with springs, contact with k_1, contact with k_2), $\Delta \in \{\mathrm{Vc0}, \mathrm{Vcp}, \mathrm{Vcn}\}$ (capsule stationary, forward motion, backward motion), $\Theta \in \{\mathrm{NCb}, \mathrm{Cb1}, \mathrm{Cb2}\}$ (no contact with fold, contact with fold with force $F_{\mathrm{b}1}$ on, contact with fold with force $F_{\mathrm{b}2}$ on) and $\Gamma \in \{\mathrm{ON}, \mathrm{OFF}\}$ (forcing on, forcing off). For instance, the operation mode $\{\mathrm{Ck2}, \mathrm{Vcp}, \mathrm{Cb1}, \mathrm{OFF}\}$ means that the capsule is moving forward with the inner mass in contact with the spring k_2, the capsule is in contact with the fold with force $F_{\mathrm{b}1}$ on and the external excitation is off. In this way, the capsule system can operate under 54 different modes, as defined in Table 4.

Table 4: Operation modes of the capsule-fold system and the corresponding values of the discrete variables H_{k_1}, H_{k_2}, H_{vel}, H_{b1}, H_{b2} and f_e defined in (23)–(28). The table lists the modes for $f_e = 0$. The modes for $f_e = 1$ are defined analogously.

Operation mode	f_e	H_{k_1}	H_{k_2}	H_{b1}	H_{b2}	H_{vel}
{NCk, Vc0, NCb, OFF}	0	0	0	0	0	0
{NCk, Vcp, NCb, OFF}	0	0	0	0	0	1
{NCk, Vcn, NCb, OFF}	0	0	0	0	0	-1
{NCk, Vc0, Cb1, OFF}	0	0	0	1	0	0
{NCk, Vcp, Cb1, OFF}	0	0	0	1	0	1
{NCk, Vcn, Cb1, OFF}	0	0	0	1	0	-1
{NCk, Vc0, Cb2, OFF}	0	0	0	0	1	0
{NCk, Vcp, Cb2, OFF}	0	0	0	0	1	1
{NCk, Vcn, Cb2, OFF}	0	0	0	0	1	-1
{Ck1, Vc0, NCb, OFF}	0	1	0	0	0	0
{Ck1, Vcp, NCb, OFF}	0	1	0	0	0	1
{Ck1, Vcn, NCb, OFF}	0	1	0	0	0	-1
{Ck1, Vc0, Cb1, OFF}	0	1	0	1	0	0
{Ck1, Vcp, Cb1, OFF}	0	1	0	1	0	1
{Ck1, Vcn, Cb1, OFF}	0	1	0	1	0	-1
{Ck1, Vc0, Cb2, OFF}	0	1	0	0	1	0
{Ck1, Vcp, Cb2, OFF}	0	1	0	0	1	1
{Ck1, Vcn, Cb2, OFF}	0	1	0	0	1	-1
{Ck2, Vc0, NCb, OFF}	0	0	1	0	0	0
{Ck2, Vcp, NCb, OFF}	0	0	1	0	0	1
{Ck2, Vcn, NCb, OFF}	0	0	1	0	0	-1
{Ck2, Vc0, Cb1, OFF}	0	0	1	1	0	0
{Ck2, Vcp, Cb1, OFF}	0	0	1	1	0	1
{Ck2, Vcn, Cb1, OFF}	0	0	1	1	0	-1
{Ck2, Vc0, Cb2, OFF}	0	0	1	0	1	0
{Ck2, Vcp, Cb2, OFF}	0	0	1	0	1	1
{Ck2, Vcn, Cb2, OFF}	0	0	1	0	1	-1

3. Interpretation of the numerical results

3.1. Two-parameter bifurcation analysis

In this subsection, the numerical results of the two-parameter bifurcation analysis of the capsule-fold dynamics under four different fold cases (see Tables 2 and 3) will be presented. Firstly, the GPU parallel computing technique [36] will be applied to obtain the two-parameter transition diagrams. Then the continuation software COCO [37] will be adopted to reveal the two-parameter bifurcation curves of a specified period-one motion (involving the capsule-fold contact). Note that GPU parallel computing is just an alternative acceleration technique for the two-parameter numerical simulations, which has already been widely used in the field of nonlinear dynamics [38, 40]. In the present work, to simulate the two-parameter transition diagrams, the non-dimensional excitation amplitude A and the duty cycle ratio D were selected as bifurcation parameters, where $A \in [1, 4]$ and $D \in [0.3, 0.6]$. The two-parameter computations for all four cases were divided into 1000 by 1000 grid points with the same initial conditions chosen as

$(x_m, v_m, x_c, v_c) = (0, 0, 0, 0)$. Note that the state variables shown here are also in non-dimensional form and the tildes shown in Eq. (20) have been omitted for convenience. Also, the Poincaré map applied in this work is the stroboscopic map. After all the above initial settings, the two-parameter transition diagrams of all four cases were obtained and shown in Fig. 4. To characterise the parameter basins of different responses in Fig. 4, the period-one and period-two motions are indicated by P1(m, n) and P2(m, n), where m and n stand for the active phases of the fold contact force (see Fig. 3) at where the minimum and maximum positions of the capsule locate, respectively. It should be noted that the impacts between the inner mass and the capsule were not presented in Fig. 4 since we focused on the capsule-fold interactions only in this work. The label 'Cross' indicates the situation where the capsule robot climbs over the fold and leaves the fold eventually. While for the rest of the responses, e.g., the periodic motions with periods exceeded two, quasi-periodic motions or chaotic motions, they were all categorized as 'Others'.

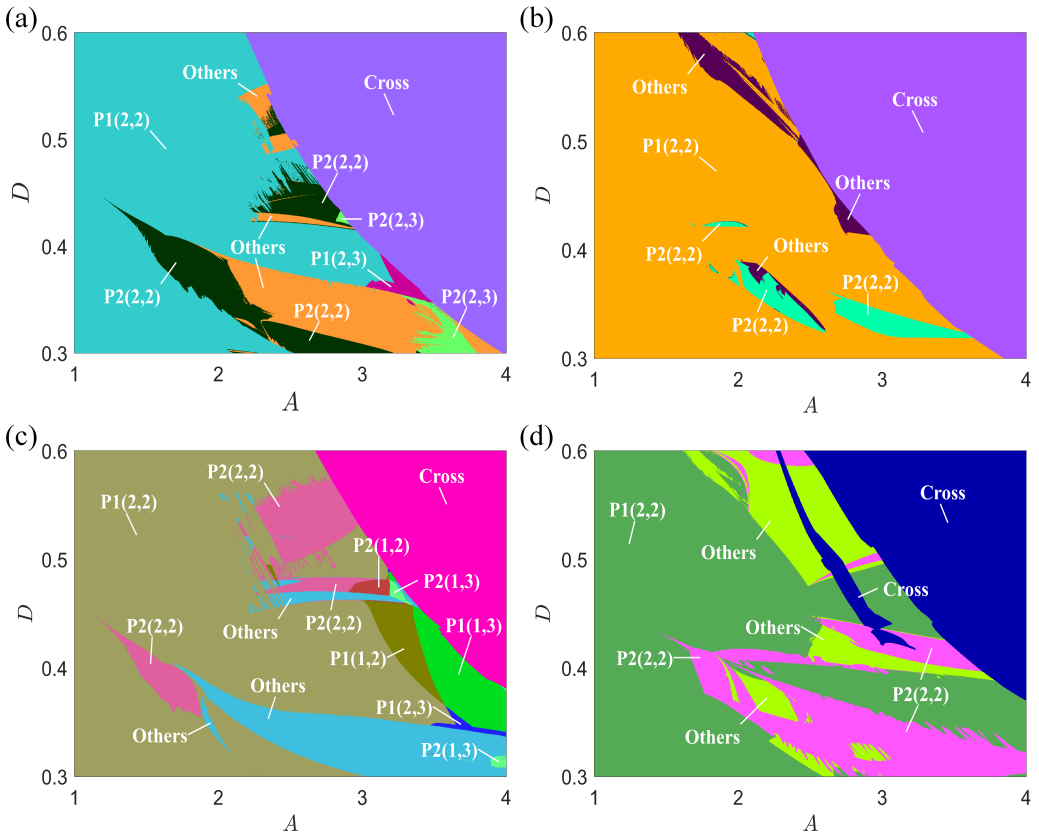

Figure 4: Two-parameter transition diagrams for (a) Case 1, (b) Case 2, (c) Case 3 and (d) Case 4 obtained by the GPU parallel computing technique. Period-one and period-two motions are indicated by label P1(m, n) and P2(m, n), where m and n stand for the active phases of the fold contact force at where the minimum and maximum positions of the capsule locate, respectively. Label 'Cross' indicates the situation where the capsule robot climbs over the fold and leaves the fold eventually. Label 'Others' stands for the rest of the responses, e.g., the periodic motions with periods exceeding two, the quasi-periodic motions, or the chaotic motions.

As can be seen from Fig. 4, the period-one motion P1$(2, 2)$ dominates the capsule-fold dynamics in all four cases when the excitation amplitude A is small, e.g., $A \in [1, 2)$. Here, the notation $(2, 2)$ in P1$(2, 2)$ means that the minimum and maximum positions of the periodic response of the capsule are both in Phase 2 of capsule-fold interaction (See Fig. 3). Under this circumstance, the capsule robot keeps squeezing the fold during the whole period. When the amplitude increases to the mid-range, e.g., $A \in (2, 3]$, the capsule responses for the four cases become more complicated than that under the small amplitude. Specifically, a diversity of steady responses including the period-two motions, the crossing

motion, and the rest motions denoted as 'Others' in the figure, emerge as the amplitude of excitation increases. However, none of these responses plays a main role within the parameter range $A \in (2, 3]$. When the amplitude is further increased to $A \in (3, 4]$, the diversity of the steady responses is weakened. In this parameter region, the crossing motion dominates the capsule-fold dynamics, which is due to the unidirectional property of the square wave excitation described in Eq. (14). As can be seen from Fig. 4, the parameter basins of the crossing motion in Cases 1 and 2 are bigger than that of Cases 3 and 4, indicating that the circular fold is easier to cross. Furthermore, more complex transitions between different period-one motions, e.g., P1$(2, 2)$, P1$(2, 3)$, P1$(1, 2)$, and P1$(1, 3)$, can be observed in the lower right corner area of Fig. 4(a) and (c), which are due to the larger Young's modulus of the circular fold.

Time history of typical capsule responses of Case 1 are presented in Fig. 5 as an example. In Fig. 5(a), the excitation parameters are chosen as $A = 1.5$ and $D = 0.34$, where a $P1(2, 2)$ stick-slip motion can be obtained, indicating the capsule keeps squeezing the circular fold at Phase 2 of capsule-fold interaction. In Fig. 5(b), the excitation parameters are specified as $A = 2$ and $D = 0.36$, where a $P2(2, 2)$ stick-slip motion is also presented. In Fig. 5(c), a period-three motion with stick-slip phenomenon is presented under the excitation parameters $A = 2.5$ and $D = 0.36$, which is categorized as 'Others' in Fig. 4. As the excitation amplitude and duty cycle are increased to $A = 3$ and $D = 0.5$, the capsule overcomes the fold's resistant force and climbs over the fold quickly.

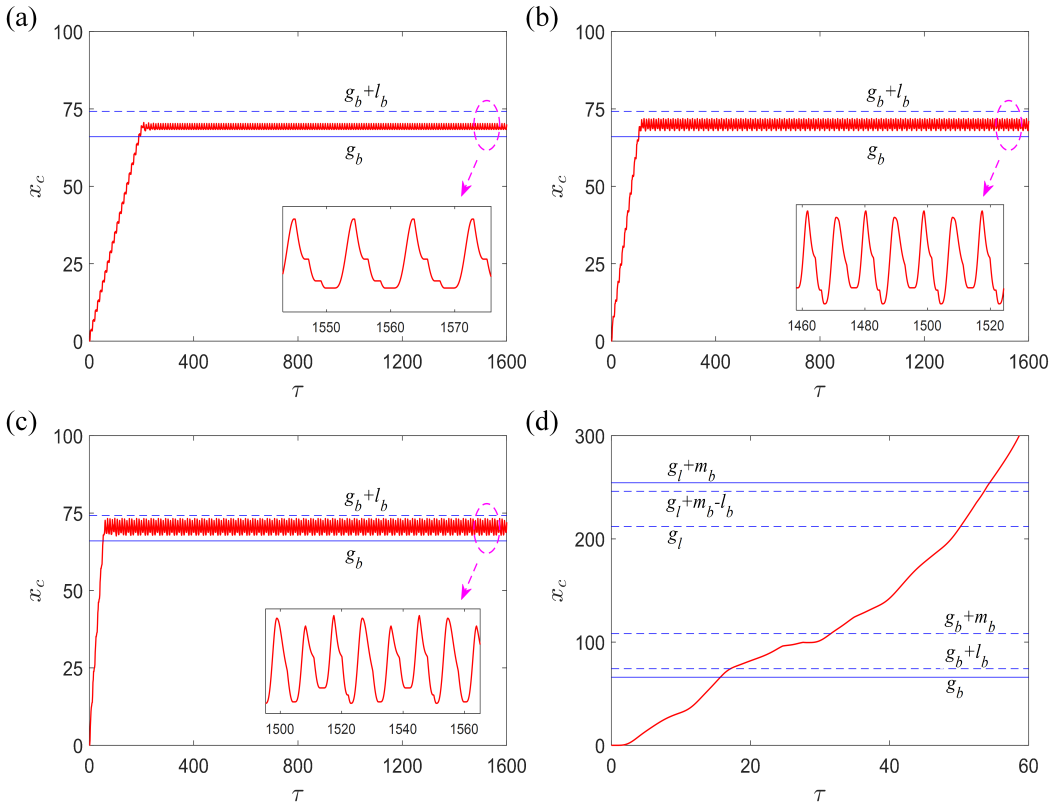

Figure 5: Time histories of typical capsule responses of Case 1. (a) $P1(2, 2)$ motion under $A = 1.5$ and $D = 0.34$; (b) $P2(2, 2)$ motion under $A = 2$ and $D = 0.36$; (c) period-three motion under $A = 2.5$ and $D = 0.36$; and (d) crossing motion under $A = 3$ and $D = 0.5$. Labels g_b, $g_b + l_b$, $g_b + m_b$, g_l, $g_l + m_b - l_b$ and $g_l + m_b$ denote the different phases of capsule-fold interaction defined in Fig. 3.

Regarding the bifurcations of the period-one motions displayed in Fig. 4, they can be classified into two types in general. The first type involves the transitions between the P$1(2, 2)$ and P$2(2, 2)$ motions, which is induced by the period-doubling bifurcation. The second type occurs between the period-one motion and the other steady responses, which is caused by the saddle-node or the Neimark-Sacker bifurcations. Since the two-parameter results shown in Fig. 4 were obtained by fixing the initial conditions as

$(x_m, v_m, x_c, v_c) = (0, 0, 0, 0)$, the boundaries of the parameter basins might not always stay the same with the bifurcation curves due to the existence of multistabiliy. Therefore, individual bifurcation analysis is required to further reveal the bifurcations of the P1(2, 2) motions and demonstrate their instability mechanisms. For this purpose, the continuation analysis software COCO was applied, and the corresponding bifurcation curves were demonstrated in Fig. 6. As can be seen from Fig. 6, the saddle-node curve is marked by the red line, the period-doubling curve is denoted by the blue line, and the Neimark-Sacker curve is indicated by a black line.

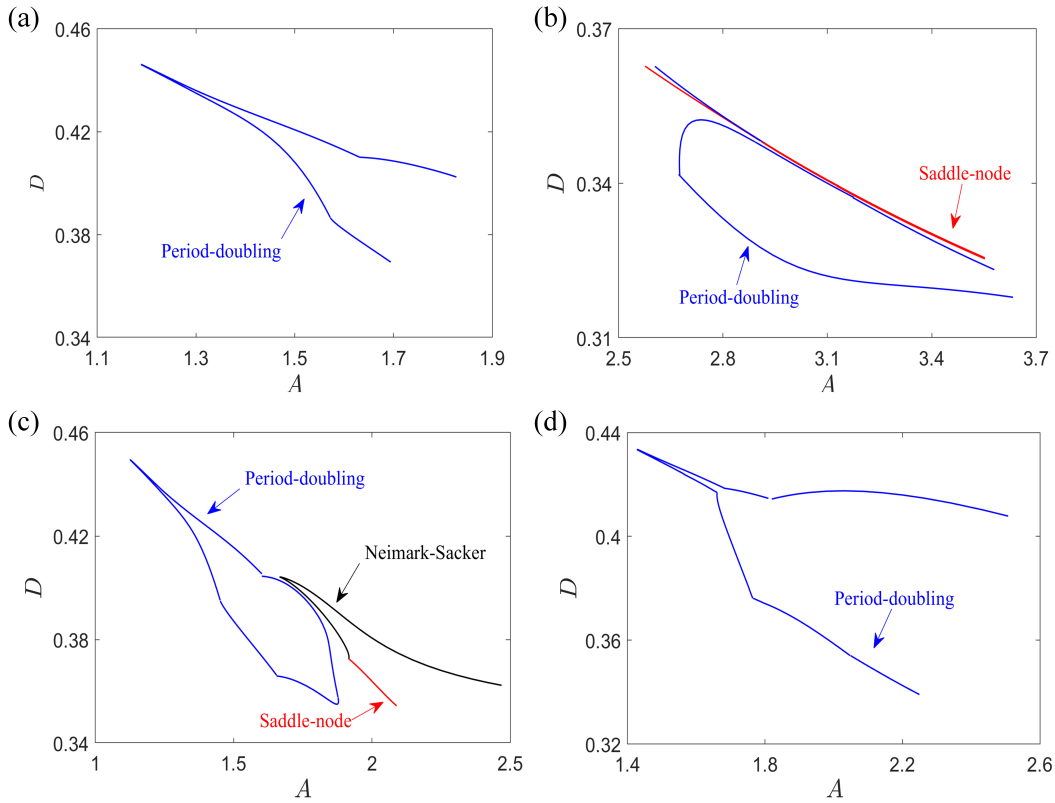

Figure 6: Two-parameter bifurcation curves of the $P1(2, 2)$ motion for (a) Case 1; (b) Case 2; (c) Case 3; and (d) Case 4 obtained by the continuation software COCO. The saddle-node bifurcation is denoted by the red line, the period-doubling bifurcation is marked by a blue line, and the Neimark-Sacker bifurcation is indicated by a black line.

For Case 1, the obtained period-doubling bifurcation curve is presented in Fig. 6(a). A noticeable feature of the curve can be captured, i.e., the sharp folding boundaries corresponding to the P2(2, 2) motion in Fig. 4(a). Regarding the unknown details about the transitions between the P1(2, 2) motion and the other type responses in Fig. 4(a), they will be studied by one-parameter analysis in the next subsection. For Case 2, the bifurcation curves of the P1(2, 2) motion is presented in Fig. 6(b). As can be seen from Fig. 6(b), a saddle-node bifurcation curve was found, in addition to the expected period-doubling curve. From an overall aspect, the detected bifurcation curves have a good agreement with the boundaries of the parameter basins of the P2(2, 2) motion shown in Fig. 4(b), and the interplay between the bifurcation curves of saddle-node and period-doubling might be due to the existence of a potential co-dimension two bifurcation point. However, the verification for the existence of such a co-dimension two bifurcation point will be very difficult in this complicated dynamical system. Also, it should be noted that the detected results of these two bifurcation curves are both incomplete due to the complexity of the capsule-fold system. For Case 3 which corresponds to a higher and stiffer fold, the bifurcation curves for the P1(2, 2) motion are shown in Fig. 6(c), where the period-doubling, the saddle-node, and the Neimark-Sacker bifurcations were all detected. In this case, a closed structure of the period-doubling bifurcation was obtained, showing a good agreement with the basin boundaries displayed in Fig. 4(c).

In addition, the interplay between the bifurcation curves of saddle-node and Neimark-Sacker might be caused by the existence of a potential co-dimension two $1:1$ resonance point. Finally, for Case 4 which corresponds to a higher but softer fold, the period-doubling bifurcation curve of the P1$(2,2)$ motion is presented in Fig. 6(d). As can be seen from this figure, the period-doubling bifurcation curve is also consistent with the basin boundaries of the P2$(2,2)$ motion shown in Fig. 4(d).

3.2. One-parameter bifurcation scenarios

In this subsection, a detailed one-parameter bifurcation analysis will be carried out in the forms of both continuation and bifurcation diagrams to better understand the two-parameter numerical results shown in Fig. 4 and Fig. 6. For such a purpose, three operating scenarios by using different duty cycles of excitation $D = 0.34$, $D = 0.4$ and $D = 0.5$ were chosen. In all the continuation diagrams, the stable branches of the P1$(2,2)$ motions are marked by red solid lines, while the unstable branches are denoted by blue dashed lines. All the detected saddle-node, period-doubling and Neimark-Sacker bifurcation points are denoted by red, blue and black squares, respectively. For the presentation of bifurcation diagrams, the results obtained by forward parameter sweep are indicated by black dots. For the backward sweep, the corresponding results are denoted by red dots. For each parameter sweep, the initial condition was chosen as $(x_{\mathrm{m}}, v_{\mathrm{m}}, x_{\mathrm{c}}, v_{\mathrm{c}}) = (0,0,0,0)$, and a path-following operation on the initial condition will be applied if the capsule reaches a bounded response, e.g., an oscillation of the capsule in contact with the circular fold without any crossing motion. While for the crossing response, the initial condition will be reset to $(x_{\mathrm{m}}, v_{\mathrm{m}}, x_{\mathrm{c}}, v_{\mathrm{c}}) = (0,0,0,0)$ for computing the next parameter grid, and no result will be plotted for the current grid in the bifurcation diagram.

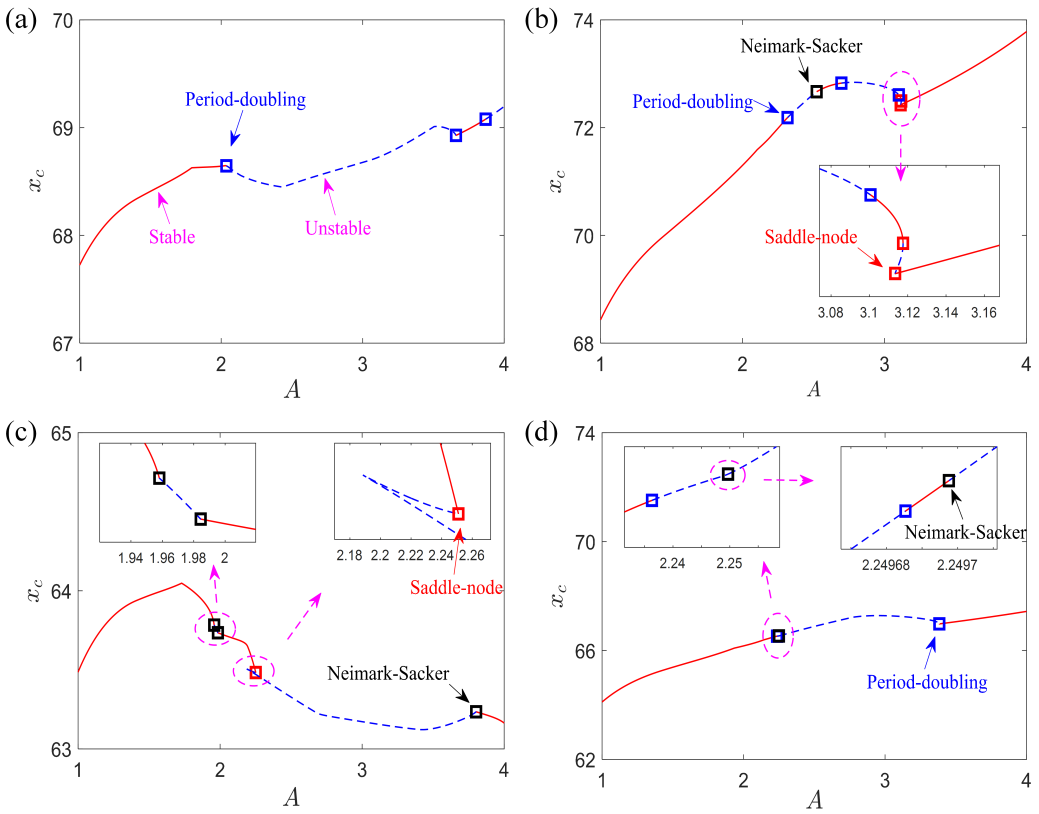

Figure 7: One-parameter continuation analysis of the $P1(2,2)$ motion with $D = 0.34$ for the four fold cases. The stable segment is denoted by the red solid line, while the unstable one is marked by the blue dashed line. The saddle-node point is denoted by a red square, the period-doubling point is marked by a blue square, while the Neimark-Sacker point is indicated by a black square. (a) Case 1; (b) Case 2; (c) Case 3; (d) Case 4.

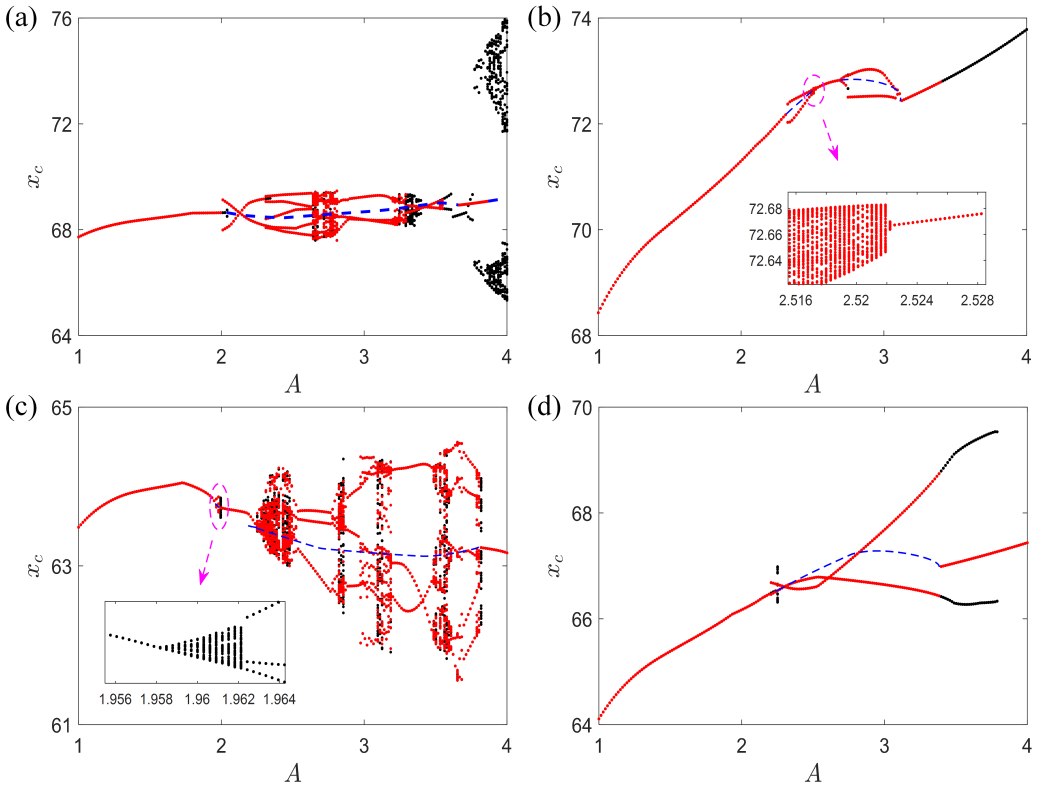

Figure 8: One-parameter bifurcation diagrams with $D = 0.34$ for the four fold cases. The forward parameter sweep result is denoted by a black dot, while the backward sweep is marked by a red dot. The blue dashed line in the four diagrams stands for the unstable result of the continuation analysis, while the red solid line indicates the stable result obtained from continuation. (a) Case 1; (b) Case 2; (c) Case 3; (d) Case 4.

Scenario 1: D = 0.34

To fully reveal the bifurcation of the P1(2, 2) motions in Fig. 4 and Fig. 6, the one-parameter continuation diagrams for four fold cases and $D = 0.34$ are shown in Fig. 7 firstly. The continuation diagram shown in Fig. 7(a) is for Case 1, where three period-doubling bifurcation points (blue squares) for $A \approx 2.0365$, 3.6595, and 3.8689 are detected. More specifically, the period-doubling bifurcation for $A \approx 2.0365$ is supercritical, generating P2(2, 2) motion. This P2(2, 2) response then encounters two saddle-node bifurcations for $A \approx 2.0402$ and 2.0039, leading to the coexistence of two independent P2(2, 2) motions, and coexistence of P1(2, 2) and P2(2, 2) motions, respectively. Details of these coexistences can be found in the bifurcation diagram in Fig. 8(a) or verified by further continuation analysis of the P2(2, 2) motion. The other two period-doubling bifurcations for $A \approx 3.6595$ and 3.8689 are still subcritical, which induces the coexistence of P1(2, 2) and fold crossing motions.

The continuation diagram for Case 2 is displayed in Fig. 7(b), showing two saddle-node bifurcations (red squares) for $A \approx 3.1135$ and 3.1176, three period-doubling bifurcations (blue squares) for $A \approx 2.3171$, 2.6961 and $A \approx 3.1006$, and one Neimark-Sacker bifurcation (black square) for $A \approx 2.5221$. The corresponding bifurcation diagram reveals that all of the period-doubling bifurcations are supercritical, but the Neimark-Sacker one is subcritical. The continuation diagram for Case 3 in Fig. 7(c) displays one saddle-node bifurcations (red squares) for $A \approx 2.2510$, and three Neimark-Sacker bifurcations (black squares) for $A \approx 1.9581$, 1.9844, and 3.8027. More specifically, the Neimark-Sacker bifurcation for $A \approx 1.9581$ is supercritical, but the other two are subcritical. In the case of the subcritical Neimark-Sacker bifurcations, there is a jump between the P1(2, 2) and chaotic motions, and long periodic motions also shows up. In Fig. 7(d), the bifurcation diagram for Case 4 has three period-doubling bifurcations (blue squares) for $A \approx 2.2363$, 2.24969, and 3.3835, and one Neimark-Sacker bifurcation (black square)

for $A \approx 2.2497$. The period-doubling bifurcations for $A \approx 2.2363$ and 3.3835 are subcritical, leading to the coexistence of P1$(2,2)$ and P2$(2,2)$ motions. However, the period-doubling and Neimark-Sacker bifurcations for $A \approx 2.2497$ are very hard to be identified because they are too close to each other, which may induce co-dimension two $1:2$ resonance.

The bifurcation diagrams obtained by numerical simulation with bidirectional parameter sweep corresponding to the continuation results in Fig. 7 are shown in Fig. 8, with all the unstable segments and partial stable segments of the continuation results of the $P1(2,2)$ motion added for better understanding. For Case 1 in Fig. 8(a), the P1$(2,2)$ motion bifurcates into P2$(2,2)$ via supercritical period-doubling, which jumps onto another P2$(2,2)$ branch via saddle-node bifurcation (black dots). Corresponding multistability phenomena can be observed in the range of $A \in (2.0402, 2.0039)$. After that, transitions between different attractors will be quite complicated in the region where the P1$(2,2)$ motion loses its stability. And multistability phenomena, i.e., coexistence between different periodic motions or between periodic and chaotic motions, can be observed as well. What should be noted is that the second stable branch of P1$(2,2)$ motion shown in Fig. 7(a) is not captured in Fig. 8(a). Instead, another supercritical period-doubling of the P1$(2,2)$ motion at $A \approx 3.72$ is newly observed (black dots). And coexistence between the bounded (black dots only) and fold crossing motions are observed for $A \in (3.563, 4]$. For Case 2 in Fig. 8(b), the transitions between different attractors stay in step with the continuation results shown in Fig. 7(b). It should be noted that the period-doubling bifurcation for $A \approx 2.3171$ is supercritical, which induces P2$(2,2)$ motion in a very small region before it transits into another P2$(2,2)$ motion. There are two kinds of multistability in Fig. 8(b), and the first kind is induced by the saddle-node bifurcations leading to the coexistence between two stable P2$(2,2)$ motions or two P2$(2,2)$ motions, respectively. By contrast, the second type of multistability is the coexistence between bounded (black dots only) and fold crossing motions in case of large excitation amplitude. For Cases 3 and 4 in Fig. 8(c)-(d), the transitions between different attractors stay in step with the continuation results in Fig. 7(c)-(d) as well. What should be noted is that the Neimark-Sacker bifurcation for $A \approx 1.9581$ in Fig. 8(c) is supercritical, but the region is too small for observation. Regarding the multistability, Fig. 7(c) shows the coexistence of P1$(2,2)$ and chaotic motions or of the P1$(2,2)$ and long periodic motions induced by subcritical Neimark-Sacker bifurcations. By contrast, Fig. 7(d) shows the coexistence of P1$(2,2)$ and P2$(2,2)$ motions induced by the combined effects of subcritical period-doubling bifurcations of the P1$(2,2)$ motion and the saddle-node bifurcations of the P2$(2,2)$ motion. However, the coexistence of bounded and fold crossing, which has been observed in Fig. 8(a)-(b), does not arise in Fig. 8(c)-(d).

Scenario 2: D = 0.4

For the second scenario ($D = 0.4$), the one-parameter continuation of the P1$(2,2)$ motion for four cases is presented in Fig. 9. In Fig. 9(a), Case 1 undergoes two saddle-node bifurcations (red squares) for $A \approx 2.1226$ and 2.1377, one period-doubling bifurcation (blue square) for $A \approx 1.5316$, and two Neimark-Sacker bifurcations for $A \approx 1.8754$ and 3.2806. This period-doubling bifurcation is subcritical to yield unstable P2$(2,2)$ motion, which will collide with another stable P2$(2,2)$ motion via saddle-node bifurcation for $A \approx 1.5156$, leading to the coexistence of stable P1$(2,2)$ and P2$(2,2)$ motions. By contrast, both of the two Neimark-Sacker bifurcations are supercritical to induce continuous transitions between P1$(2,2)$ and quasi-periodic motions. For Case 2 shown in Fig. 9(b), a simple bifurcation pattern with only two saddle-node bifurcations (red squares) for $A \approx 1.9677$ and 2.0095 is observed. In Fig. 9(c), Case 3 displays two saddle-node bifurcations (red squares) for $A \approx 1.8809$ and 1.8950, three period-doubling bifurcation (blue square) for $A \approx 1.4374$, 1.7117 and 3.8571, and two Neimark-Sacker bifurcations (black squares) for $A \approx 1.7276$ and 1.7564. Except for the subcritical period-doubling bifurcation for $A \approx 1.4374$, both of the other two period-doubling bifurcations are supercritical. The Neimark-Sacker bifurcations at $A \approx 1.7276$ and $A \approx 1.7564$ are subcritical and supercritical, respectively. For Case 4 in Fig. 9(d), one can observe one saddle-node bifurcation (red square) for $A \approx 2.5022$, and six period-doubling bifurcations (blue squares) for $A \approx 1.6956$, 1.9463, 2.0070, 2.0131, 2.7523 and 2.8685. Except for the subcritical one for $A \approx 2.0131$, the other five period-doubling bifurcations are all supercritical.

Corresponding bifurcation diagrams obtained by numerical simulations are displayed in Fig. 10, showing the transitions between different attractors consistent with the continuation results in Fig. 9. Case 1 in Fig. 10(a) shows three types of the multistability phenomena. Firstly, the coexistence of stable

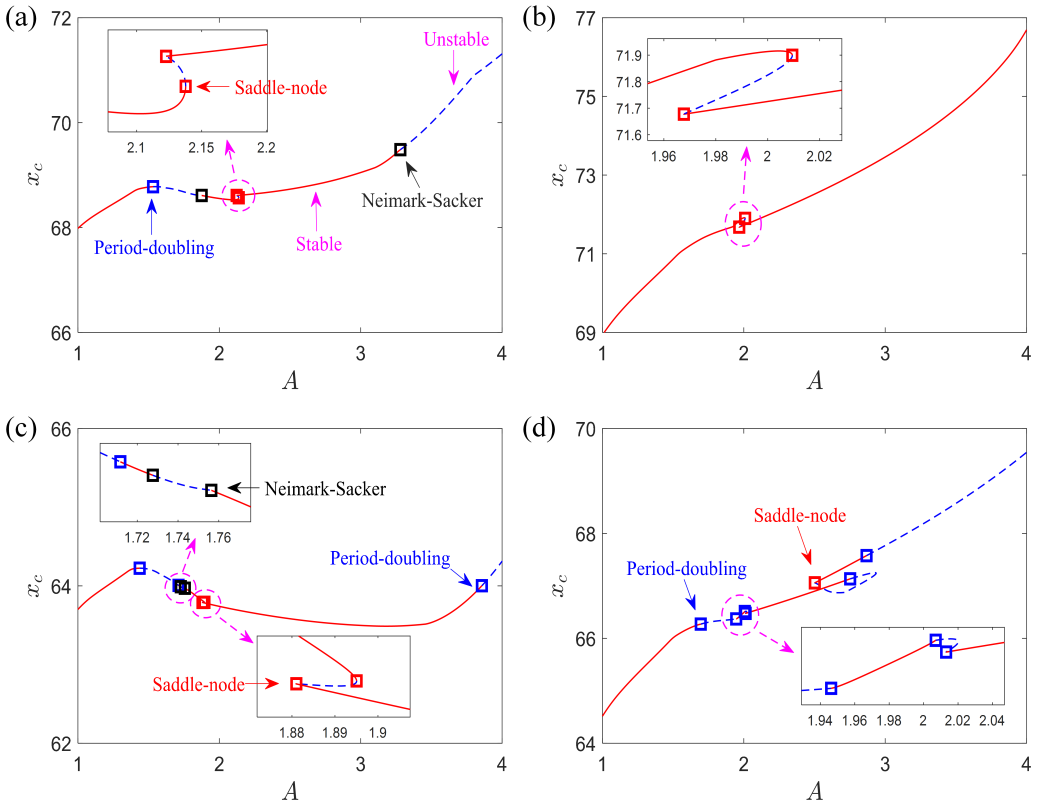

Figure 9: One-parameter continuation analysis of the $P1(2,2)$ motion with $D = 0.4$ for the four fold cases. The stable segment is denoted by the red solid line, while the unstable one is marked by the blue dashed line. The saddle-node point is denoted by a red square, the period-doubling point is marked by a blue square, while the Neimark-Sacker point is indicated by a black square. (a) Case 1; (b) Case 2; (c) Case 3; (d) Case 4.

P1(2, 2) and P2(2, 2) motions induced by the combined effects of the subcritical period-doubling bifurcation of the P1(2, 2) motion and the saddle-node bifurcation of the P2(2, 2) motion can be observed in the small neighborhood of the subcritical period-doubling bifurcation for $A \approx 1.5316$. Secondly, coexistence between two stable P1(2, 2) motions can be observed near the saddle-node bifurcation for $A \approx 2.1226$ and 2.1377. Thirdly, coexistence between the bounded and cross motions can be observed in the large amplitude region, with only the bounded motions (black dots) plotted. It should be noted that the quasi-periodic motions induced by the supercritical Neimark-Sacker bifurcation for $A \approx 1.8754$ arise only in a very small range and are therefore hard to be observed. For Case 2 shown in Fig. 10(b), two kinds of multistability phenomena can be observed, where the first is the coexistence of two stable P1(2, 2) motions near two saddle-node bifurcations and the second multistability is the coexistence of P1(2, 2) and fold crossing motions in the large amplitude region.

Three types of multistability are observed in Fig. 10(c) for Case 3. The first is the coexistence of stable P1(2, 2) and P2(2, 2) motions, which is induced by the combined effects of the subcritical period-doubling bifurcation of the P1(2, 2) motion and the saddle-node bifurcation of the P2(2, 2) motion. The second is the coexistence of two stable P1(2, 2) motions induced by two saddle-node bifurcations. The third type is the coexistence of P1(2, 2), P2(2, 2) and fold crossing motions in the large amplitude region.

The bifurcation in Fig. 10(d) for Case 4 shows a complex pattern with six period-doubling bifurcations of the P1(2, 2) motion. The first kind of multistability involves a closed structure of the P2(2, 2) motion near the period-doubling bifurcations for $A \approx 2.0070$ and 2.0131. This P2(2, 2) motion then encounters saddle-node bifurcations, leading to the coexistence of P1(2, 2) and P2(2, 2) motions and of two independent P2(2, 2) motions. However, such multistability phenomena exist only in a very small range which is hard to be observed. The second type of multistability involves both the closed structure of the P2(2, 2)

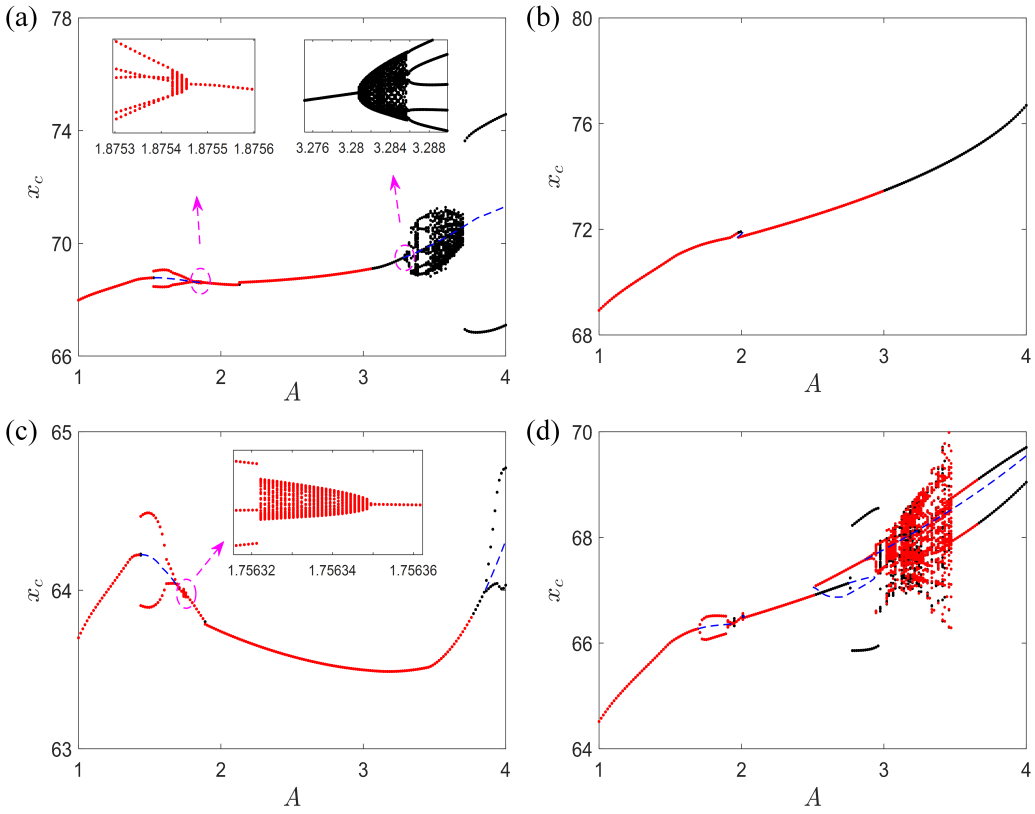

Figure 10: One-parameter bifurcation diagrams with $D = 0.4$ for the four fold cases. The forward parameter sweep result is denoted by a black dot, while the backward sweep is marked by a red dot. The blue dashed line in the four diagrams stands for the unstable result of the continuation analysis, while the red solid line indicates the stable result obtained from continuation. (a) Case 1; (b) Case 2; (c) Case 3; (d) Case 4.

motion and the fold structure of the P1$(2, 2)$ motion for $A \in (2.5022, 2.9738)$. This closed structure of the P2$(2, 2)$ motion encounters saddle-node bifurcations as well, leading to complicated multistability phenomena. In the region of large excitation amplitude, there is the third type of multistability, the coexistence of P2$(2, 2)$ and the crossing motions.

Scenario 3: D = 0.5

Next, the one-parameter continuation results of the P1$(2, 2)$ motion for the four cases are presented in Fig. 11 for the scenario of $D = 0.5$. The continuation diagram of Case 1 in Fig. 11(a) displays a saddle-node bifurcation (red square) for $A \approx 2.3858$, and two period-doubling bifurcations (blue squares) for $A \approx 2.7109$ and 2.9831. Both of the two period-doubling bifurcations are supercritical, but the one for $A \approx 2.7109$ arises only in a very small range and is therefore hard to be observed.

In Fig. 11(b), Case 2 shows three saddle-node bifurcations (red squares) for $A \approx 2.3715$, 2.3933 and 3.4297, and two period-doubling bifurcations (blue squares) for $A \approx 2.4163$ and 3.3479. The period-doubling bifurcation for $A \approx 2.4163$ is supercritical, inducing response only in a very small range, which is hard to be observed. The period-doubling bifurcation for $A \approx 3.3479$ is subcritical, yielding a P2$(2, 2)$ motion to encounter a saddle-node bifurcation for $A \approx 3.3813$ to jump onto another stable P2$(2, 2)$ branch. Case 3 in Fig. 11(c) detects one saddle-node bifurcation (red square) for $A \approx 2.4507$, and two period-doubling bifurcations (blue squares) for $A \approx 2.5353$ and 3.5553. The period-doubling bifurcation for $A \approx 2.5353$ is subcritical, inducing unstable P2$(2, 2)$ motion, which will encounter a saddle-node bifurcation for $A \approx 2.5483$ and jump onto another stable P2$(2, 2)$ branch. The period-doubling bifurcation for $A \approx 3.5553$ is supercritical for a continuous transition from the stable P1$(2, 2)$ motion to P2$(2, 2)$. Case 4 in Fig. 11(d) has one saddle-node bifurcation (red square) for $A \approx 2.3467$, and one Neimark-Sacker

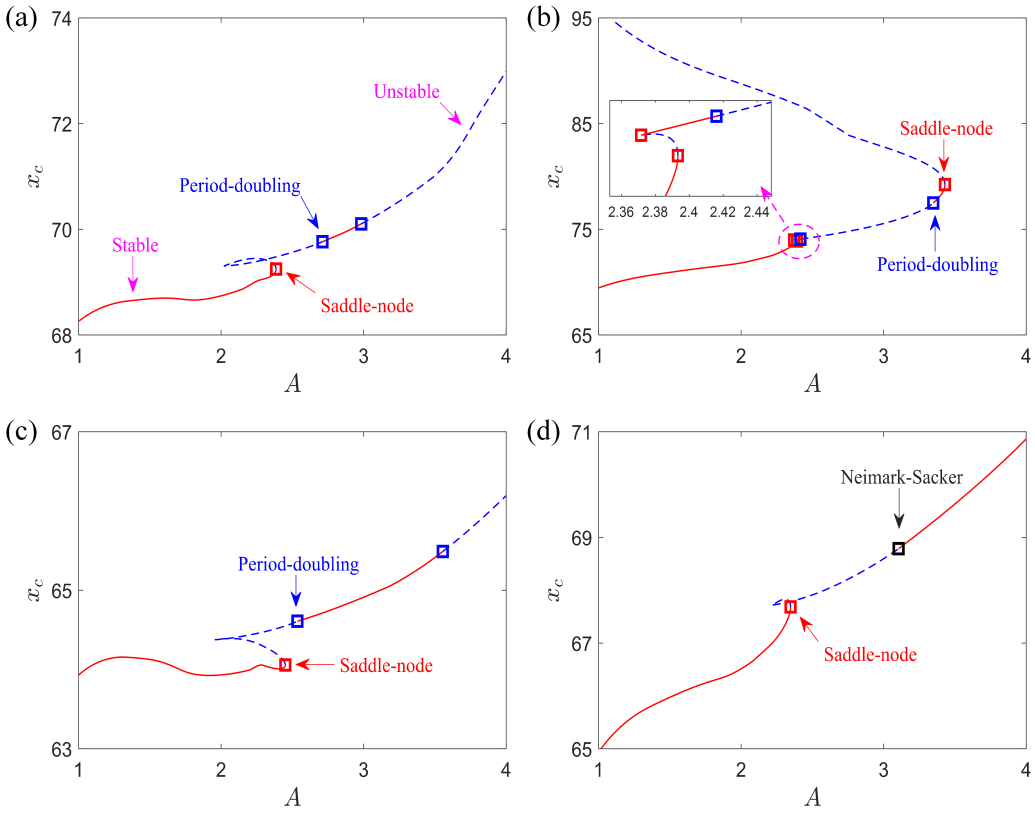

Figure 11: One-parameter continuation analysis of the $P1(2,2)$ motion with $D = 0.5$ for the four fold cases. The stable segment is denoted by a red solid line, while the unstable one is marked by the blue dashed line. The saddle-node point is denoted by a red square, the period-doubling point is marked by a blue square, while the Neimark-Sacker point is indicated by a black square. (a) Case 1; (b) Case 2; (c) Case 3; (d) Case 4.

bifurcation (black square) for $A \approx 3.1047$. The Neimark-Sacker bifurcation is supercritical, yielding a quasi-periodic motion in a very small range.

Next, the bifurcation diagrams obtained by numerical simulations are presented in bifurcation diagrams for the four cases with $D = 0.5$ as displayed in Fig. 12, showing transitions between different attractors in step with the continuation results shown in Fig. 11. Regarding the multistability in Fig. 12(a)-(d), one expects the coexistence of bounded and fold crossing motions in the regions of large amplitude excitation. Compared with the previous scenarios, the starting point of this kind of multistability for $D = 0.5$ is much lower than those for $D = 0.34$ and 0.4. Besides, the multistability, coexistence of the $P1(2,2)$ and $P2(2,2)$ (or the follow-up chaotic) motions, induced by saddle-node bifurcation of the $P1(2,2)$ can be observed in Fig. 12(a) as well. In Fig. 12(b), the multistability is due to the combined effects of the subcritical period-doubling bifurcation of the $P1(2,2)$ motion and the saddle-node bifurcation of the $P2(2,2)$ motion, yielding the coexistence of $P1(2,2)$ and $P2(2,2)$ motions. In Fig. 12(c), the bifurcation induced multistability are more complicated than the previous two cases. In addition to the multistability induced by the saddle-node bifurcations of the $P1(2,2)$ motion or the $P2(2,2)$ motion (bifurcated from the subcritical period-doubling bifurcation), the bifurcations of the $P2(2,2)$ motion on the special 'X' type structure (from $A \approx 2.1156$ to 2.8543) also contribute to the multistability mechanism. Note that such special 'X' type structure of the $P2(2,2)$ motion might be in a closed form, but the continuation of this structure is quite difficult.

3.3. Basin stability analysis and typical basins of attraction

In the previous subsection, the multistability phenomena and related mechanisms arising in the above bifurcation diagrams are primarily summarized. According to the bifurcation analysis, it can be found

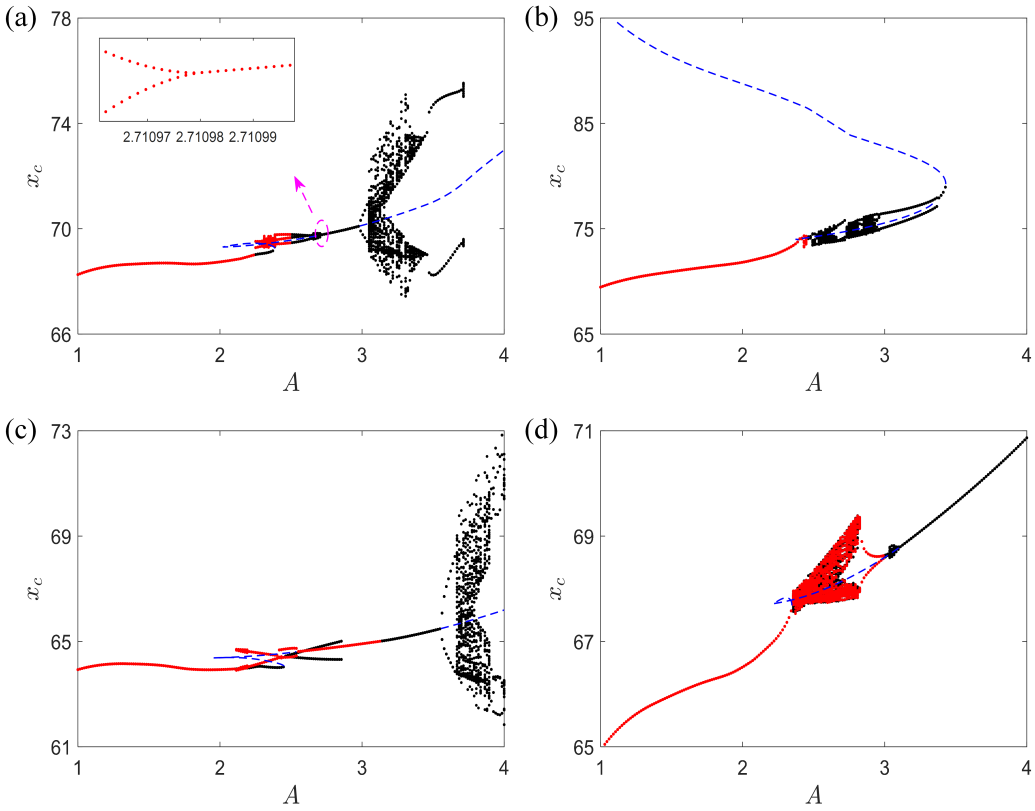

Figure 12: One-parameter bifurcation diagrams with $D = 0.5$ for the four fold cases. The forward parameter sweep result is denoted by a black dot, while the backward sweep is marked by a red dot. The blue dashed line in the four diagrams stands for the unstable result of the continuation analysis, while the red solid line indicates the stable result obtained from continuation. (a) Case 1; (b) Case 2; (c) Case 3; (d) Case 4.

that the bifurcations of saddle-node bifurcation, subcritical period-doubling, and subcritical Neimark-Sacker all contribute to the multistability. However, the bifurcation analysis does not provide global aspects of the dynamics of the capsule-fold system. To better uncover the multistability and evaluate the locomotion of the capsule robot, the basin stability analysis will be conducted. Indeed, such basin stability analysis can quantify the stability of given attractors from a probability aspect, by randomly choosing initial conditions from certain ranges [41–43]. Focusing on a random manner rather than a deterministic manner of the initial conditions, the basin stability method shows an advantage over the classical method of using basins of attraction when analysing the multidimensional system. Note that the classical basins of attraction method will also be employed here to demonstrate the influence of initial conditions on the steady responses for some typical bifurcation scenarios. To calculate the measure of basin stability, i.e., the probability of reaching a given attractor, a significant number of Bernoulli trials should be simulated and the final attractors reached in each trial should be classified. Under the condition of randomly initial conditions in a specified range, the probability that the system can reach the attractor $\mathcal{A}$ is given by $p(\mathcal{A})$. Then the classical definition of probability $p(\mathcal{A})$ can be written as [41–43],

$$p(\mathcal{A}) = N(\mathcal{A})/N \tag{29}$$

where $N(\mathcal{A})$ indicates the number of trials leading to the given attractor $\mathcal{A}$, and N denotes the total number of trials. Meanwhile, the multi-degree-of-freedom cell mapping method [38] is adopted here to further accelerate the simulations of Bernoulli trials and calculation of the typical basins of attraction as well. In what follows, the results of the one-parameter basin stability analysis for three scenarios, i.e., $D = 0.34$, 0.4 and 0.5 for four fold cases, will be presented in Figs. 13-15. To perform such analysis,

15 different values of A will be uniformly chosen from $A \in [1, 4]$ for each case. For accurate estimation of probability $p(\mathcal{A})$, a large number $N = 10000$ of initial conditions will be randomly chosen from the following space.

$$\Sigma_1 = \left\{ (x_{\rm r}, v_{\rm r}, x_{\rm c}, v_{\rm c}) \in R^4 | -4 \le x_{\rm r} \le 4, -4 \le v_{\rm r} \le 4, 0 \le x_{\rm c} \le 60, -4 \le v_{\rm c} \le 4 \right\} \tag{30}$$

It should be noted that the relative variables $(x_{\rm r}, v_{\rm r})$ instead of the mass variables $(x_{\rm m}, v_{\rm m})$ are considered here to avoid the unreasonable settings on the relative displacement and velocity.

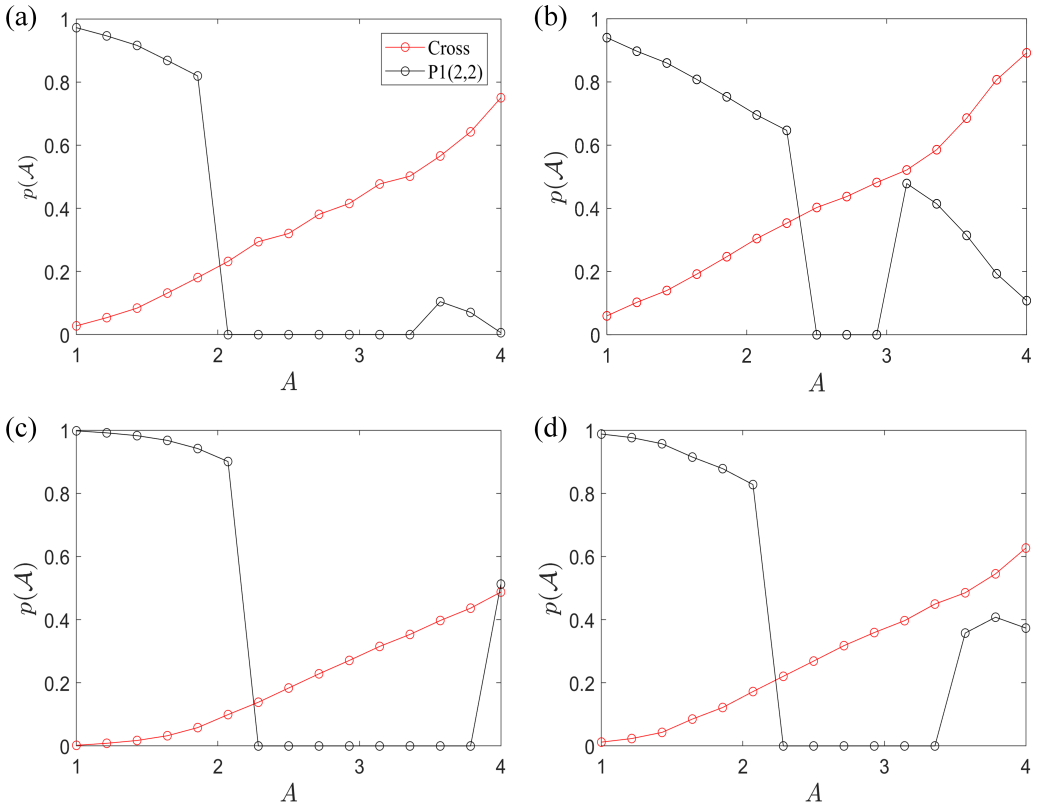

Figure 13: One-parameter basin stability analysis for the four fold cases with $D = 0.34$. Note that $p(\mathcal{A})$ denotes the occurrence probability of the fold cross or the P1(2, 2) motions. (a) Case 1; (b) Case 2; (3) Case 3; (4) Case 4.

For Scenario 1 with $D = 0.34$, the one-parameter basin stability analysis for the four fold cases is shown in Fig. 13 as functions of A. In this and the following two figures, the probabilities of reaching two basic responses, i.e., P1(2, 2) and fold crossing motions, are respectively presented by black and red lines with circles. By contrast, the other stable motions gaining too small probabilities of occurrence are not illustrated in the diagrams, due to the frequent secondary bifurcations. The probability of fold crossing motion keeps non-zero in Fig. 13, which reaches its minimum, 0.0021, for $A = 1$ in Fig. 13(c). In general, the tendencies of fold crossing are similar among the four cases, which keeps increasing with the excitation amplitude. Particularly, the probability of fold crossing for Case 2 is obviously bigger than in any other case, indicating that a smaller softer fold increases the probability of crossing. On the contrary, the largest toughest fold in Case 3 has the smallest probability of fold crossing, which is less than 50% in the large amplitude region.

The P1(2, 2) motion dominates the region for $A < 2$ in Fig. 13, but its occurrence decreases rapidly with the increase of amplitude A. Once the P1(2, 2) motion loses its stability, the probability becomes zero in a band. However, the P1(2, 2) motion regains its stability through bifurcation in the large amplitude region. It should be noted that the band of zero probability of the P1(2, 2) motion would not be exactly

the same as the results of continuation and bifurcation diagrams, due to the sparse sampling operation. Meanwhile, the transitions of the P1(2, 2) motion can be complicated in the large amplitude region in both of Figs 13(a) and (c). In Fig. 13(a), the P1(2, 2) motion for $A \approx 3.5714$ with a probability of 0.1045 locates on the same branch with the P1(2, 2) motion for $A = 4$ with a probability of 0.0062. However, this branch of P1(2, 2) motion has not been captured in Fig. 7(a), although has been partially observed in Fig. 8(a). By contrast, the P1(2, 2) motion for $A \approx 3.7857$ with a probability of 0.0704 has been captured by the continuation analysis and in Fig. 7(a). In Fig. 13(c), there are two stable P1(2, 2) motions for $A = 4$ with probabilities of 0.4942 and 0.0183, respectively. However, the one with a low probability has not been captured in the continuation analysis as well. All these features indicate that the global dynamics of the capsule-fold system are quite complicated and a basin stability analysis is necessary.

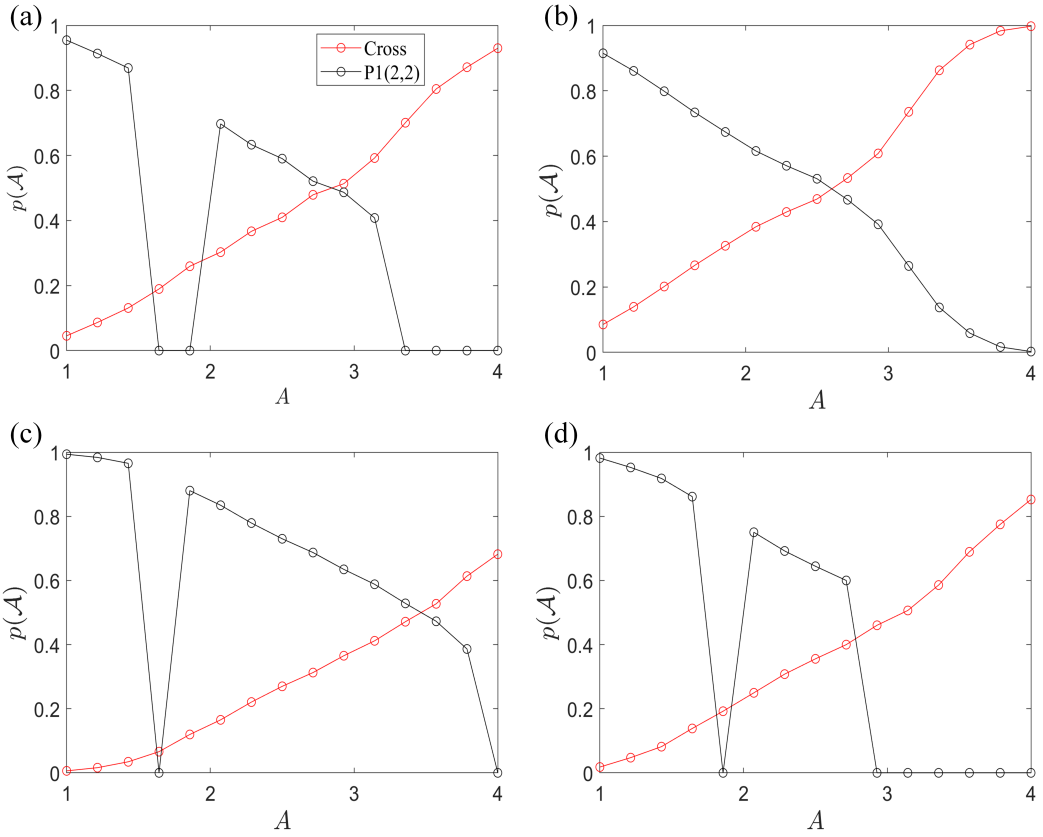

Figure 14: One-parameter basin stability analysis for the four fold cases with $D = 0.4$. $p(\mathcal{A})$ denotes the occurrence probability of the fold cross or the P1(2, 2) motions. (a) Case 1; (b) Case 2; (3) Case 3; (4) Case 4.

The results of the one-parameter basin stability analysis of Scenarios 2 and 3, $D = 0.4$ and 0.5, are respectively shown in Figs. 14-15 as functions of A, where the probabilities of P1(2, 2) and fold crossing motions are indicated by black and red lines with circles, respectively. As can be seen in both figures, the probability of the fold crossing motion increases with the amplitude A to dominate the capsule-fold dynamics near $A = 4$ for all four cases. Moreover, it can be seen that a higher duty cycle D leads to a higher probability of fold crossing motion. By contrast, the P1(2, 2) motion dominates the dynamics in the region of small amplitude A and its probability decreases rapidly with respect to the increase of A. Then a band of zero probability arises due to bifurcations of P1(2, 2) motion.

It should be noted that the global dynamics of the four cases show great differences in the zero probability band of the P1(2, 2) motion. To present such complexity, $D = 0.34$ and $A = 2.5$ in Fig. 13(a)-(d) is taken as an illustrative example. With these parameters, the fold crossing motion (probability 0.3204) coexists with a period-five attractor (probability 0.6796) in Case 1. In Case 2, the fold crossing

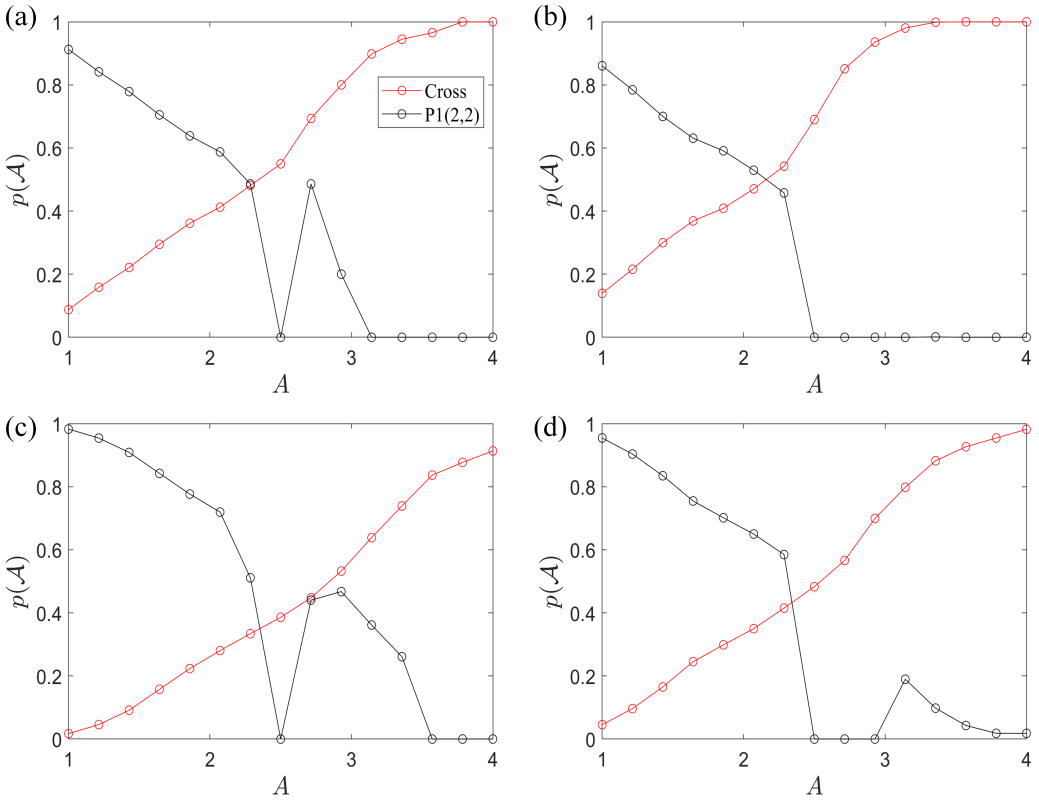

Figure 15: One-parameter basin stability analysis for the four fold cases with $D = 0.5$. $p(\mathcal{A})$ denotes the occurrence probability of the fold cross or the P1(2, 2) motions. (a) Case 1; (b) Case 2; (3) Case 3; (4) Case 4.

motion (probability 0.4027) coexists with a chaotic response (probability 0.5973). In Case 3, the fold crossing motion (probability 0.1835) coexists with a period-six attractor (probability 0.4341) and a period-twelve attractor (probability 0.3824). In Case 4, the fold crossing motion (probability 0.2688) coexists with a period-two attractor (probability 0.7312). Corresponding basins of attraction are displayed in Figs 16(a)-(d), respectively, with the initial condition plane specified as follows.

$$\Sigma_2 = \left\{(x_{\rm r}, v_{\rm r}, x_{\rm c}, v_{\rm c}) \in R^4 | -4 \le x_{\rm r} \le 4, -4 \le v_{\rm r} \le 4, x_{\rm c} = 0, v_{\rm c} = 0\right\} \tag{31}$$

The initial condition plane is divided into 500×500 cells in Fig. 16(a)-(d). As can be seen in Fig. 16, the basin of attraction of the fold crossing motion (blue) is always on the left side. The coexisting attractors are on the right side and marked by yellow or baby blue colors. It should be noted that the probabilities of attractors obtained by basin stability analysis and basin of attraction analysis show a big difference. For example, probabilities of cross motion obtained by basin stability analysis for the four fold cases are 0.3204, 0.4027, 0.1835, and 0.2688, respectively. While the results obtained by the basin of attraction analysis are 0.3602, 0.3856, 0.2982, and 0.3361, respectively. The reason is that a two-dimensional initial condition plane cannot fully reveal the dynamical information of the full initial condition space. Despite the numerical differences, it can be seen that such diversity in multistability shows the potential to distinguish the four fold cases.

4. Conclusions

This paper studied the dynamics of a vibro-impacting self-propelled capsule robot in contact with a circular fold, when moving in the small intestine for endoscopic diagnosis. The robot, modeled as

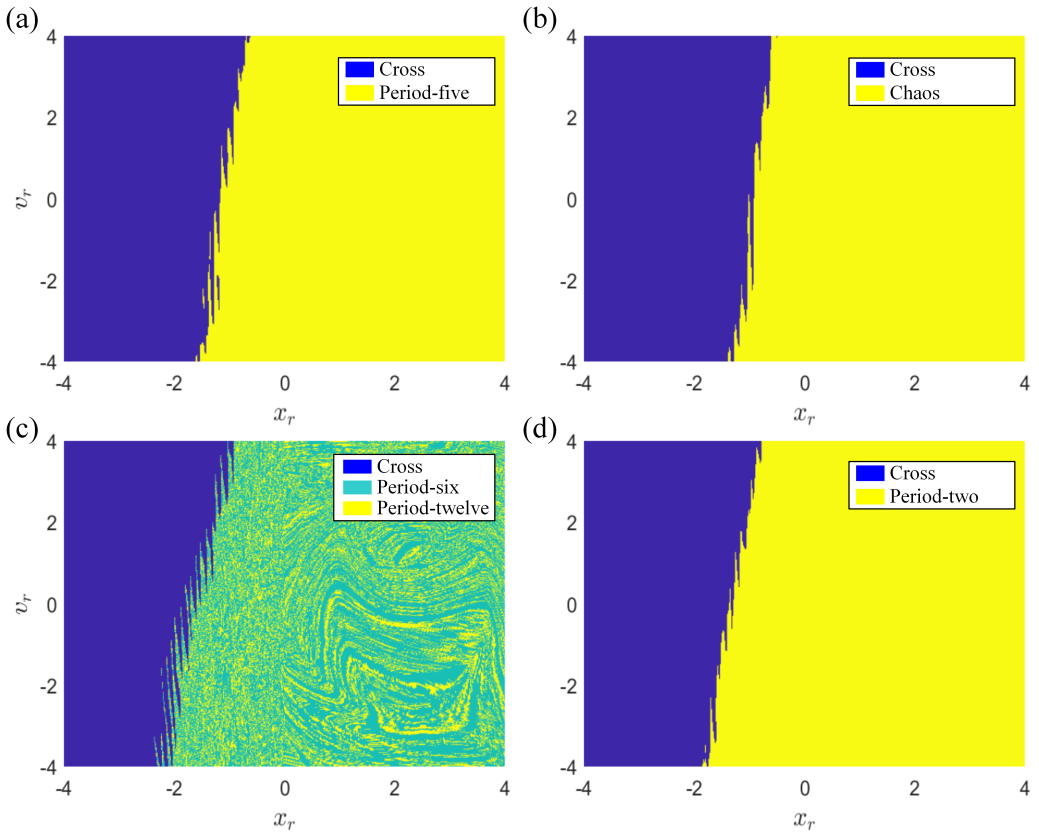

Figure 16: Typical basins of attraction for the four fold cases with $D = 0.34$ and $A = 2.5$. (a) Case 1; (b) Case 2; (3) Case 3; (4) Case 4.

a non-smooth dynamical system, was periodically driven by an inner mass interacting with the main body of the capsule. The resistant force of the intestine, in particular, when the capsule was in contact with the circular fold (a permanent structure of the intestinal lining), was modeled mathematically and simplified by approximating it with piecewise polynomials for the convenience of numerical analysis. The aim of this study was to understand the dynamics of the capsule robot when encountering different types of circular folds in terms of dimension and rigidity. By using the GPU parallel computing and path-following techniques, a two-parameter bifurcation analysis was conducted firstly to provide an initial view of the capsule-fold dynamics under four fold cases with different heights, widths, and rigidity. Two elementary attractors, the $P1(2,2)$ motion and the crossing motion, were observed in the transition diagrams obtained by the GPU computing technique. For the $P1(2,2)$ motion, a period-one oscillation with the capsule sticking to the fold was observed for all four cases when the excitation amplitude of the capsule robot was small. As the amplitude of excitation increased, the crossing motion of the robot was recorded. Thus, the preliminary boundaries of crossing motions were identified for locomotion control of the robot in the small intestine. From a practical point of view, $P1(2,2)$ is our desired motion because of its simplicity and stability, and the less the complexity of transitions before the crossing motion is, the easier the required control is. Comparing the capsule-fold dynamics under four fold cases, it was found that the parameter basin of the crossing motion for Case 2 (corresponding to a smaller and softer circular fold) was the largest, and its complexity of transitions was the least. This finding indicates that both the excitation parameters (e.g., the excitation amplitude and duty cycle) and the mechanical properties of the fold have significant influences on the capsule-fold dynamics. It also indicates that a smaller and softer circular fold is easier to be crossed. Thereafter, the two-parameter bifurcation curves obtained by path-following techniques further revealed and confirmed the primary instability mechanisms of the

$P1(2,2)$ motion for all the four fold cases.

To better understand the two-parameter numerical results, a detailed one-parameter bifurcation analysis was performed. The results revealed some further details on the bifurcations of the $P1(2,2)$ motion. It was found that such complicated bifurcation behaviours led to the diversity of the bifurcating responses and various bifurcation-induced multistability phenomena, e.g., the multistability induced by the combined effects of the saddle-node and the period-doubling bifurcations. Meanwhile, the one-parameter numerical results further confirmed the significant influence from both the excitation parameters and the fold properties on the capsule-fold dynamics. In general, the one- and two-parameter bifurcation results can provide essential guidance for the locomotion control of the self-propelled capsule robot in the small intestine, when a circular fold is encountered.

Considering the fact that bifurcation analysis can only provide local information on the dynamics of the vibro-impacting capsule, this work further conducted the basin stability analysis to characterise the capsule-fold dynamics from a global perspective. The results showed that the $P1(2,2)$ motion dominated the global dynamics of the system with a high probability for all the four fold cases when the excitation amplitude of the robot was small. It should be noted that the crossing motion coexisted with the $P1(2,2)$ motion in the small amplitude region, but with a very low probability. Indeed, such a coexistence cannot be easily revealed by the bifurcation analysis, proving the necessity of global analysis. Regarding the large amplitude region, the crossing motion can gain a high probability, and therefore, dominated the global dynamics of the system. In practice, we prefer to maintain this high probability for the crossing motion as the transit time of the capsule robot in the small intestine should be as short as possible. It was also found that the probability of the crossing motion of Case 2 was obviously higher than that of the other three cases. This indicates that a smaller and softer circular fold may increase the probability of crossing, while a larger and stiffer fold will induce more complex dynamics in the capsule robot. In addition, a significant change in multistability was also observed at certain parameters, and such a correlation between the multistability and the fold's properties could be used to distinguish various types of circular folds.

For future work, the influences of the fold's shape and the excitation parameters of the robot on the capsule-fold dynamics will be further investigated. In particular, the bump that mimics an early bowel cancer will be mathematically modeled in contact with the capsule robot. Also, machine learning techniques, e.g., [13, 19], might be used for locomotion control of the capsule robot in the presence of different circular folds in the small intestine.

Acknowledgments

This project has received funding from the European Union's Horizon 2020 research and innovation programme under the Marie Skłodowska-Curie grant agreement No [101018793]. Professor Yao Yan would like to acknowledge the financial support from National Natural Science Foundation of China (Grants No. 11872147, and 12072068).

Compliance with ethical standards.

Conflict of interest. The authors declare that they have no conflict of interest concerning the publication of this manuscript.

Data accessibility. The numerical data sets generated and analysed during the current study are available from the corresponding author on reasonable request.

References

[1] J. Xu and H. Fang, "Improving performance: recent progress on vibration-driven locomotion systems," *Nonlinear Dynamics*, vol. 98, no. 4, pp. 2651–2669, 2019.

[2] B. Guo, Y. Liu, R. Birler, and S. Prasad, "Self-propelled capsule endoscopy for small-bowel examination: proof-of-concept and model verification," *International Journal of Mechanical Sciences*, vol. 174, p. 105506, 2020.

[3] M. Liao, M. Wiercigroch, M. Sayah, and J. Ing, "Experimental verification of the percussive drilling model," *Mechanical Systems and Signal Processing*, vol. 146, p. 107067, 2021.

[4] C. Dengqing, B. Kunchao, D. Hu, Z. Xubin, P. Zhongwen, C. Liqun, and Z. Shige, "Advances in dynamics and vibration control of large-scale flexible spacecraft," *Chinese Journal of Theoretical and Applied Mechanics*, vol. 51, no. 1, p. 1, 2019.

[5] C. Ma, L. Gao, T. Xin, X. Cai, M. M. Nadakatti, and P. Wang, "The dynamic resonance under multiple flexible wheelset-rail interactions and its influence on rail corrugation for high-speed railway," *Journal of Sound and Vibration*, vol. 498, p. 115968, 2021.

[6] A. Colombo, M. Di Bernardo, S. Hogan, and M. Jeffrey, "Bifurcations of piecewise smooth flows: Perspectives, methodologies and open problems," *Physica D: Nonlinear Phenomena*, vol. 241, no. 22, pp. 1845–1860, 2012.

[7] O. Makarenkov and J. S. Lamb, "Dynamics and bifurcations of nonsmooth systems: A survey," *Physica D: Nonlinear Phenomena*, vol. 241, no. 22, pp. 1826–1844, 2012.

[8] S. Wang, L. Hong, and J. Jiang, "Analytical prediction on stick-slip whirling oscillations induced by dry friction between a rotating imbalanced rotor and a flexibly supported stator," *Journal of Sound and Vibration*, vol. 511, p. 116333, 2021.

[9] O. P. Yadav, S. R. Balaga, and N. S. Vyas, "Forced vibrations of a spring–dashpot mechanism with dry friction and backlash," *International Journal of Non-Linear Mechanics*, vol. 124, p. 103500, 2020.

[10] G. Stefani, M. De Angelis, and U. Andreaus, "Numerical study on the response scenarios in a vibro-impact single-degree-of-freedom oscillator with two unilateral dissipative and deformable constraints," *Communications in Nonlinear Science and Numerical Simulation*, vol. 99, p. 105818, 2021.

[11] G. Stefani, M. De Angelis, and U. Andreaus, "Influence of the gap size on the response of a single-degree-of-freedom vibro-impact system with two-sided constraints: Experimental tests and numerical modeling," *International Journal of Mechanical Sciences*, vol. 206, p. 106617, 2021.

[12] G. Stefani, M. De Angelis, and U. Andreaus, "Scenarios in the experimental response of a vibro-impact single-degree-of-freedom system and numerical simulations," *Nonlinear Dynamics*, vol. 103, no. 4, pp. 3465–3488, 2021.

[13] K. O. Afebu, Y. Liu, E. Papatheou, and B. Guo, "Lstm-based approach for predicting periodic motions of an impacting system via transient dynamics," *Neural Networks*, vol. 140, pp. 49–64, 2021.

[14] B. E. Saunders, R. Vasconcellos, R. Kuether, and A. Abdelkefi, "Characterization and interaction of geometric and contact/impact nonlinearities in dynamical systems," *Mechanical Systems and Signal Processing*, vol. 167, p. 108481, 2022.

[15] S. Li, H. Wu, X. Zhou, T. Wang, and W. Zhang, "Theoretical and experimental studies of global dynamics for a class of bistable nonlinear impact oscillators with bilateral rigid constraints," *International Journal of Non-Linear Mechanics*, vol. 133, p. 103720, 2021.

[16] X.-F. Geng, H. Ding, X.-Y. Mao, and L.-Q. Chen, "Nonlinear energy sink with limited vibration amplitude," *Mechanical Systems and Signal Processing*, vol. 156, p. 107625, 2021.

[17] E. J. Staunton and P. T. Piiroinen, "Discontinuity mappings for stochastic nonsmooth systems," *Physica D: Nonlinear Phenomena*, vol. 406, p. 132405, 2020.

[18] D. J. Simpson, V. Avrutin, and S. Banerjee, "Nordmark map and the problem of large-amplitude chaos in impact oscillators," *Physical Review E*, vol. 102, no. 2, p. 022211, 2020.

[19] Z. Tan, S. Yin, G. Wen, Z. Pan, and X. Wu, "Near-grazing bifurcations and deep reinforcement learning control of an impact oscillator with elastic constraints," *Meccanica*, pp. 1–20, 2022.

[20] P. E. Dupont, B. J. Nelson, M. Goldfarb, B. Hannaford, A. Menciassi, M. K. O'Malley, N. Simaan, P. Valdastri, and G.-Z. Yang, "A decade retrospective of medical robotics research from 2010 to 2020," *Science Robotics*, vol. 6, no. 60, p. eabi8017, 2021.

[21] F. N. Alsunaydih and M. R. Yuce, "Next-generation ingestible devices: sensing, locomotion and navigation," *Physiological Measurement*, vol. 42, no. 4, p. 04TR01, 2021.

[22] J. Xue, S. Zhang, and J. Xu, "Coordinated optimization of locomotion velocity and energy consumption in vibration-driven system," *Meccanica*, pp. 1–15, 2022.

[23] B. Guo, E. Ley, J. Tian, J. Zhang, Y. Liu, and S. Prasad, "Experimental and numerical studies of intestinal frictions for propulsive force optimisation of a vibro-impact capsule system," *Nonlinear Dynamics*, vol. 101, no. 1, pp. 65–83, 2020.

[24] K. Madani, S. Khanmohammadi, and V. Azimirad, "Finding optimal actuation configuration for magnetically driven capsule endoscopy based on genetic algorithm," *Journal of Medical and Biological Engineering*, vol. 36, no. 6, pp. 776–787, 2016.

[25] B. Kim, S. Park, C. Y. Jee, and S.-J. Yoon, "An earthworm-like locomotive mechanism for capsule endoscopes," in *2005 IEEE/RSJ International Conference on Intelligent Robots and Systems*, pp. 2997–3002, IEEE, 2005.

[26] H. Park, S. Park, E. Yoon, B. Kim, J. Park, and S. Park, "Paddling based microrobot for capsule endoscopes," in *Proceedings 2007 IEEE International Conference on Robotics and Automation*, pp. 3377–3382, IEEE, 2007.

[27] M. Quirini, A. Menciassi, S. Scapellato, C. Stefanini, and P. Dario, "Design and fabrication of a motor legged capsule for the active exploration of the gastrointestinal tract," *IEEE/ASME transactions on mechatronics*, vol. 13, no. 2, pp. 169–179, 2008.

[28] K.-T. Nguyen, N.-T. La, K.-T. Ho, Q.-H. Ngo, N.-H. Chu, and V.-D. Nguyen, "The effect of friction on the vibro-impact locomotion system: modeling and dynamic response," *Meccanica*, vol. 56, no. 8, pp. 2121–2137, 2021.

[29] M. Liao, J. Zhang, Y. Liu, and D. Zhu, "Speed optimisation and reliability analysis of a self-propelled capsule robot moving in an uncertain frictional environment," *International Journal of Mechanical Sciences*, vol. 221, p. 107156, 2022.

[30] Y. Liu, M. Wiercigroch, E. Pavlovskaia, and H. Yu, "Modelling of a vibro-impact capsule system," *International Journal of Mechanical Sciences*, vol. 66, pp. 2–11, 2013.

[31] Y. Liu, E. Pavlovskaia, D. Hendry, and M. Wiercigroch, "Vibro-impact responses of capsule system with various friction models," *International Journal of Mechanical Sciences*, vol. 72, pp. 39–54, 2013.

[32] Y. Liu, E. Pavlovskaia, M. Wiercigroch, and Z. Peng, "Forward and backward motion control of a vibro-impact capsule system," *International Journal of Non-Linear Mechanics*, vol. 70, pp. 30–46, 2015.

[33] Y. Liu, J. Páez Chávez, J. Zhang, J. Tian, B. Guo, and S. Prasad, "The vibro-impact capsule system in millimetre scale: numerical optimisation and experimental verification," *Meccanica*, vol. 55, no. 10, pp. 1885–1902, 2020.

[34] L. J. Sliker, G. Ciuti, M. E. Rentschler, and A. Menciassi, "Frictional resistance model for tissue-capsule endoscope sliding contact in the gastrointestinal tract," *Tribology International*, vol. 102, pp. 472–484, 2016.

[35] Y. Yan, B. Zhang, Y. Liu, and S. Prasad, "Dynamics of a vibro-impact self-propelled capsule encountering a circular fold in the small intestine," *Meccanica*, 2022, https://doi.org/10.1007/s11012-022-01528-2.

[36] N. Ploskas and N. Samaras, *GPU programming in MATLAB*. Morgan Kaufmann, 2016.

[37] H. Dankowicz and F. Schilder, *Recipes for continuation*. Computational Science and Engineering, Philadelphia: SIAM, 2013.

[38] S. Yin, G. Wen, J. Ji, and H. Xu, "Novel two-parameter dynamics of impact oscillators near degenerate grazing points," *International Journal of Non-Linear Mechanics*, vol. 120, p. 103403, 2020.

[39] L. Barducci, J. Norton, S. Sarker, S. Mohammed, R. Jones, P. Valdastri, and B. Terry, "Fundamentals of the gut for capsule engineers," *Progress in Biomedical Engineering*, vol. 2, p. 042002, 2020.

[40] R. Zeng, G. Wen, J. Zhou, and G. Zhao, "Limb-inspired bionic quasi-zero stiffness vibration isolator," *Acta Mechanica Sinica*, vol. 37, no. 7, pp. 1152–1167, 2021.

[41] P. J. Menck, J. Heitzig, N. Marwan, and J. Kurths, "How basin stability complements the linear-stability paradigm," *Nature physics*, vol. 9, no. 2, pp. 89–92, 2013.

[42] P. Brzeski and P. Perlikowski, "Sample-based methods of analysis for multistable dynamical systems," *Archives of Computational Methods in Engineering*, vol. 26, no. 5, pp. 1515–1545, 2019.

[43] Y. Liu, J. Páez Chávez, P. Brzeski, and P. Perlikowski, "Dynamical response of a rocking rigid block," *Chaos: An Interdisciplinary Journal of Nonlinear Science*, vol. 31, no. 7, p. 073136, 2021.